Measurement of Properties of the Lunar Surface Using the Diviner Lunar Radiometer Experiment on the NASA Lunar Reconnaissance Orbiter

Ian Thomas

Second Year Report

Lincoln College

Atmospheric, Oceanic and Planetary Physics

University of Oxford

August 2009

Supervised by Dr. Neil Bowles and Dr. Simon Calcutt

Contents

1 Introduction....8
2 Lunar Properties....9
2.1 Formation of the Moon....9
2.2 The Lunar Surface....10
2.3 Surface Temperature....11
2.3.1 Permanently Shaded Regions....11
2.3.2 Permanently Illuminated Regions....13
2.4 Mineralogy....13
2.4.1 Christiansen Feature....13
3 Lunar Missions....16
3.1 Previous Missions....16
3.1.1 Apollo 17, 1972....16
3.1.2 Clementine, 1994....16
3.1.3 Lunar Prospector, 1998....17
3.1.4 SMART-1, 2003....19
3.1.5 SELENE, 2007....19
3.1.6 Current Missions....19
3.1.7 Ground Based Instruments....19
3.2 The Lunar Reconnaissance Orbiter....21
3.2.1 Mission Objectives....21
3.2.2 Overview of Other Onboard Instruments....21
4 Diviner Lunar Radiometer Experiment....24
4.1 Design....24
4.2 Goals of the DLRE....24
4.3 Diviner Spectral Channels....26
5 Filter Measurements....28
5.1.1 B2 and B3 Filter Measurements....28
5.2 Short-distance Filter Measurements....28
5.2.1 Filter Holder....30
5.2.2 Choice of Detector....30
5.2.3 Detector Electronics....31
5.2.4 Accurately Determining the Detector to Filter Distance....31
5.2.5 Measurement Procedure....32
6 Laboratory Mineral Measurements....37

6.1.1 Sample Selection....37
6.2 Diffuse Reflectance....37
6.3 Specular Reflectance Measurements....45
6.4 Emission Measurements – The Lunar Environment Simulator....45
6.4.1 Initial Design....45
6.4.2 Improvements....47
6.4.3 The Final Lunar Environment Simulator....50
7 Data Analysis....52
8 Future Work....54
8.1 Continue with Emission Measurements....54
8.2 Diviner Radiometric Calibration Validation....54
8.3 Using Diviner Data and New Mineral Spectra to Model Properties of an Area of the Lunar Surface....55
9 Acknowledgements....57
10 Bibliography....58
11 Appendix....61
11.1 Bulk Parameters of the Moon and Earth....61
11.2 Orbital Parameters of the Moon....61
11.3 Properties of the Lunar Atmosphere....62
11.4 Estimated Lunar Composition....62
11.5 DLRE Specification Requirements....62
11.6 The Brüker IFS 66v Fourier Transform Spectrometer....63

List of Figures

Figure 1: The Moon, as photographed from the Northern Hemisphere of Earth, by Viatour Luc in 2006. 10

Figure 2: Model calculated diurnal lunar surface temperature variations over a complete diurnal cycle for horizontal surfaces at latitudes (from top to bottom) of 0◦, 60◦, 75◦, and 89◦ (summer) or 89◦(winter). The minimum detectable temperature of Clementine (section 3.1.2) and the DLRE instrument have been indicated [Chin et al, 2007]. 12

Figure 3: Modelled diurnal temperature curves for regolith (black) and rock (grey) in a mid latitude region, for a full lunar day (from 0 to 360°). The models were created using a 1-D Thermophysical Model written by John Spencer [Spencer, 1990]. Values used were: Albedo=0.123 (average bond albedo of the Moon), period=29.5 days (synodic period of the Moon), emissivity=0.9 (lunar average), thermal inertia=50 J m^{-2} K^{-1} $s^{-1/2}$ (regolith), 2400 J m^{-2} K^{-1} $s^{-1/2}$ (solid basalt) [Gaidos et al, 2006]. 12

Figure 4: The ratio of the emission spectra of the central highlands/Copernicus of the Moon from Murcray et al, 1970, ratioed by Lucey, 1991. The measurements were made using a radiometer from 32km above the Earth's surface, minimising the effects of atmospheric absorption. The telescope used had a large field of view of 3 arcminutes, so the spectra observed are of entire regions of the Moon. 15

Figure 5: Thermophysical modelling of the thermal gradients observed in a quartz regolith, heated by sunlight normal to the surface, for three values of thermal conductivity [Henderson and Jakosky, 1997]. Curve c was made using a value for conductivity appropriate for lunar surface minerals, with a and b more akin to conditions on Earth and Mars. 15

Figure 6: Clementine LWIR temperature data, showing gaps in coverage (left) and an enlarged view of a crater showing temperature variations of the surface, generated in IDL (right). The minimum detectable temperature of the instrument was ~200K for adequate signal to noise, and so the crater floor could not be mapped reliably. Differences in temperatures can be clearly observed. 18

Figure 7: Epithermal neutron count rate for both lunar poles, showing increased hydrogen detected at the north and south poles, with craters superimposed on the maps [Feldmann, 1998]. 18

Figure 8: An image of central peak of Shackleton Crater, taken by the Terrain Camera on SELENE [Haruyama et al, 2008]..... 20

Figure 9: Early results from the Moon Mineralogy Mapper onboard Chandrayaan-1 [Kerr (ed.), 2009]. The bright areas indicate regions of nearly pure plagioclase. 20

Figure 10: A computer generated model of LRO orbiting the Moon, with Diviner indicated by the white arrow. 22

Figure 11: The fraction of the lunar surface which will be mapped each year around noon-time, plotted as a function of the Moon's latitude [Paige et al, 2009]. 22

Figure 12: A diagram of the Diviner instrument. The instrument is positioned close to the underside of the spacecraft; hence the image has been flipped to show its true orientation with respect to the lunar surface. 25

Figure 13: A plot showing the blackbody functions of various temperatures, overlaid with the normalised DLRE filter responses. 27

Figure 14: Transmission spectrum of B2 and B3 mesh filters. Due to limitations of the Brüker FTS at small wavenumbers, the lower cut-off of the B3 filter may slightly vary in shape from the recorded spectra. These filters were measured in early 2008, prior to the radiometric calibration analysis. 29

Figure 15: Spectral response of each of the individual meshes comprising the B2 filter, as measured by the University of Cardiff, and the total transmission of the stack, measured in the Brüker IFS 66v at Oxford. 29

Figure 16: Autodesk® Inventor™ CAD drawing of the short-distance filter holder. The detector was attached to the right-hand plate, which was kept at the focus of the spectrometer beam.. 31

Figure 17: A Cadence® OrCAD™ diagram of the pre-amplification circuit constructed for the LIE-332f detector. 33

Figure 18: The results from the CMM measurements, with the xyz- coordinates (green stars) plotted in Autodesk® Inventor™. Work planes have been added to these coordinates, with the large planes representing the back plate, and the small planes representing the detector front. The angle measured between these two planes is shown. 33

Figure 19: The spectral response of the B1 channel at various filter-to-detector distances. No systematic broadening of the channel is seen as the distance is reduced, but a plateau region is observed at beyond the long-wavelength cut-off. This plateau can clearly be seen to increase as the filter-detector distance is reduced, indicating that this is likely to be a spectral leak....35

Figure 20: The B2 channel measured at various filter-to-detector distances. While there are considerable differences between the measurements of the long-wavelength cut-off, no trend is seen from smallest to greatest filter-detector distance. The differences could be due to "channelling" as can be seen throughout the entire spectra, or due to the low spectral resolution at high wavelengths....35

Figure 21: The B3 filter response at various filter-detector distances. The oscillations observed here, most likely due to channelling, are significant, therefore only the short-wavelength switch-on is shown. The lower signal in the far infrared means that the effects of channelling appear to increase with increasing wavelength, to the extent that the long-wavelength cut-off is indiscernible from these measurements 36

Figure 22: The Specac® Diffuse Selector Accessory, inside the Brüker IFS 66v sample compartment. The white arrow indicates the location of the sample under investigation. 40

Figure 23: The vacuum chamber, designed by Jon Temple and constructed by Jason Perry and Duncan Constable in the AOPP workshop. 40

Figure 24: The Brüker IFS 66v with the vacuum chamber inside the spectrometer and vacuum piping coming through the sample chamber lid 41

Figure 25: An Autodesk® Inventor™ CAD drawing of the stepper motor jig. 41

Figure 26: A photo of a new-design sample cup, containing Albite, placed in the vacuum oven at 50°C to remove water vapour from the powdered rock. The *3 indicates that this sample is composed of 0-64μm size particles, along with the sample cup number and date and time in which it was placed in the vacuum oven. The samples were smoothed to ensure a uniform, level surface for accurate reflectance measurements to be performed. 43

Figure 27: The graphs shows diffuse reflectance spectra for some of the minerals measured, with particle sizes of 64-120μm, magnified to highlight the differences in Christiansen

Feature location. The spectra were found by dividing by the diffuse Al reference and normalising to have a maximum of 1 and a minimum of 0. In general, the CF shifts to longer wavelengths with increasing abundance of mafic minerals, from Quartz to Fayalite, as expected [Salisbury et al, 1997]. 43

Figure 28: The effect of varying grain size on diffuse reflectance measurements. The band contrast is seen to reduce for increased grain sizes at the CF reflectance minima around 8.5 microns, except for the 64-120 micron grain size sample. 44

Figure 29: Combined VIS/NIR, MIR and FIR spectra across almost all of the wavelength ranges measurable by Diviner. In some regions of the spectrum, the minerals are more diffusely reflecting than the diffuse reflectance standard used, hence reflectances higher than 1 are observed. 44

Figure 30: The Perkin Elmer® Specular Reflectance Kit, placed on the custom-built apparatus, allowing it to be used upside down. The sample being measured is indicated by the white arrow. 46

Figure 31: A plot showing both diffuse and specular reflectance results. The lines have been scaled and offset in the y-direction to make the different mineral spectra distinguishable. The diffuse and specular reflectance spectra are observed to exhibit identical spectral features, though the specular features are less pronounced. 46

Figure 32: A simple ray-tracing diagram showing how the beam from the sample was expected to be reflected into the spectrometer emission port at the correct angle. 48

Figure 33: The emission apparatus after addition of the liquid nitrogen feed-through. 48

Figure 34: A simple ray-tracing diagram showing how the beam is changed by the finite width at the point of convergence and the part of the box around the hole that is included in the emission measurement. 49

Figure 35: Emission of heated and cooled quartz particulates measured by Baldridge and Christensen 2009. 49

Figure 36: The final design for the Lunar Environment Simulator. 51

Figure 37: Calibrated mid infrared spectra of Anorthite composed of 0-32 micron sized grains. The graphs have been normalised so that the Christiansen Feature emissivity peak is shown with an emissivity of 1. The graph shows that as the box is cooled, the peak is enhanced. 51

Figure 38: Some initial Diviner B3 brightness temperature data from 6th July to 12th August, split into two equal datasets, showing the south pole below -80° latitude. The variations in temperatures due to the change in local hour are visible. 53

Figure 39: A Mercator map of the Moon, showing the wavelength of the Christiansen Feature calculated by plotting a quadratic through Diviner channels A3-A5 [Paige, personal communication 2009]. The data already shows clear distinctions between the highlands (yellow, red and pink) and the mare (blue). More data taken closer to midday will improve this map significantly, especially on the far side of the Moon, where the data used to derive this map was taken at a late afternoon local hour. 53

Figure 40: The optical layout inside the Brüker IFS 66v Fourier Transform Spectrometer, with the main parts labelled. Almost all of the optional parts (dotted red line) are available. 64

List of Tables

Table 1: Properties of Diviner's Spectral Channels [Paige et al, 2009]. 27

Table 2: The minerals and mixtures, grain-size distributions and wavelength ranges that were successfully measured, where S = specular reflectance, D = diffuse reflectance, and E = emission. Some measurements could not be performed due to lack of signal (especially in the FIR or with 'dark' samples), and some were not needed.. 39

Table 3: A Gantt Chart showing approximate dates of completion for the various stages of the D.Phil Project. Expected times are shown in blue, while contingency times are shown in green.....56

Table 4: Bulk Parameters of the Moon and Earth (Data taken from the NASA National Space Science Data Centre, available from: http://nssdc.gsfc.nasa.gov/planetary/factsheet/moonfact.html). 61

Table 5: Orbital parameters, for orbit about the Earth (Data taken from NASA NSSDC). 61

Table 6: Lunar Atmospheric Properties (Data taken from NASA NSSDC). 62

Table 7: Estimated Composition of most abundant atmospheric species. Also possible traces of Phosphorus (P+), Sodium (Na+), Magnesium (Mg+) (Data taken from NASA NSSDC)..62

Table 8: The specifications of the DLRE instrument, required to be verified during pre-flight calibration [Foote, personal communication 2008]. 63

1 Introduction

The Moon is the Earth's only major natural satellite, and is a large airless body approximately one quarter the radius of the Earth. It has been speculated that the lunar poles may have the resources available to support human exploration, as permanently shaded craters exist which have been speculated to contain water ice and other volatiles. The Diviner Lunar Radiometer Experiment (DLRE), most commonly known as Diviner, was launched onboard the Lunar Reconnaissance Orbiter (LRO) on 18th June 2009, and has since successfully switched on and begun mapping the lunar surface. The LRO satellite was developed as a response to President Bush's Vision for Space Exploration in 2004, whereby a precursor mission was required to facilitate the future construction of a manned outpost on the lunar surface. The instrument is a nine-channel radiometer designed to map the temperature and certain mineralogical features of the entire surface from a low orbit, over the course of at least one year. The instrument is capable of mapping the temperature of the permanently shaded craters, which in conjunction with other instruments on board LRO, should be able to determine whether water is present in these cold surface regions. Accurate thermal mapping of the surface at various local times of day will also allow thermophysical models of the lunar regolith to be made, to determine the bulk properties of the surface; and surface emission and reflectance measurements will allow the composition of the surface to be further constrained than at present.

The LRO satellite also contains several more instruments, including a high resolution camera, a Lyman-α mapper, a neutron detector, a laser altimeter, a synthetic aperture radar, and a cosmic radiation detector. A lunar impactor, called the Lunar Crater Observation and Sensing Satellite (LCROSS) was launched together with LRO, which will also search for water by launching a rocket stage into a permanently shaded crater and then analysing the ejected plume. The impact is currently due to occur on 9th October 2009.

The second year of this project has involved continuing preparations for the interpretation of returning data, such as completing filter measurements, and measuring reflectance and emission properties of analogous lunar minerals in support of the Diviner compositional experiment [Greenhagen and Paige, 2009]. A start has been made into investigating data analysis techniques, with some analysis of data returned during commissioning orbit being performed.

2 Lunar Properties

For a manned outpost to be established on the Moon, the most important resources required are water and a constant source of power for supporting life, and minerals for construction purposes. Water can also be separated into hydrogen and oxygen, essential for fuel and sustaining life, and solar power is the most likely source of power [Jolliff et al (eds.), 2006].

Water, and hence hydrogen and oxygen, can be extracted from rocks, but this is a very energy intensive process [Jolliff et al (eds.), 2006]; therefore it would be hugely advantageous to find water ice deposits on or near the surface. The probability of water deposits being present is dependent on the areas of the lunar surface where the temperature has remained cold enough for water to have remained trapped, while the amount of solar illumination incident on a given point on the surface is dependent on the topography and the Moon's orbital properties. The distribution of minerals in the lunar crust is dependent on geological processes occurring during and since the Moon's formation.

2.1 Formation of the Moon

The Moon is thought to have been formed approximately 4.5 billion years ago, from a collision between the proto-Earth and a body of a similar size to Mars, known as 'Theia' [Benz et al, 1986]. The molten proto-planets then cooled, and were subjected to bombardment by comets and meteors, bringing new elements to the bodies of the solar system. Unlike the Earth, the Moon has insufficient mass to retain a considerable atmosphere, which results in large diurnal temperature variations between the areas of the surface under solar illumination and those in darkness. This is because no convection and very little conduction takes place, as the lunar soil (or regolith) has a low thermal conductivity [Vasavada, 1999]. Therefore, even though comets may have deposited water and other volatiles across the entire surface, any region which has ever been illuminated by the Sun will have lost the water molecules in that area due to evaporation. Also, water molecules can be lost by photo-dissociation and by collisions with particles in the solar wind.

As the Moon has a small obliquity (the difference in angle between the rotational plane of the Moon's spin axis and the ecliptic plane) of 1.54°, at the lunar poles are craters which currently reside in permanent darkness, and are believed to have been like this for many billions of years [Ward, 1975; Mignard, 1979]. In these cold traps, water and other volatiles may still be present, and possibly in sufficient amounts to support a manned outpost on the Moon. The obliquity history of the Moon is very important, as it will determine the amount, if any, of water-ice present. If there was a period in the past where the rotational axis deviated from the ecliptic plane by more than approximately 30° then no large-scale permanent cold traps can have existed at that point; if this event happened within the past few billion years then probability of detecting water from orbit is significantly reduced [Watson et al, 1961 & Arnold, 1979].

Due to frictional forces in the Earth-Moon system, the Moon is tidally locked, meaning that one side of the Moon remains facing the Earth throughout its orbit. Therefore the diurnal period of the Moon (i.e. one lunar day) is equal to its synodic period of 29.5 Earth days. The temperature of the surface varies tremendously during a lunar day, typically from below 100K to over 350K for mid- and low- latitude regions, due to the trace atmosphere (Appendix Table 6).

Figure 1: The Moon, as photographed from the Northern Hemisphere of Earth, by Viatour Luc in 2006.

2.2 The Lunar Surface

Lunar materials can be classified into three generations, depending on their age and amount of time exposed to incoming particles and radiation from space [Jolliff et al (eds), 2006]:

1. First Generation: These are old plutonic and volcanic igneous rocks unaffected by impacts, and are formed from molten material. Plutonic (or intrusive) refers to material which solidified beneath the lunar surface, and volcanic (or extrusive) refers to material which solidified on the surface. Examples include Anorthosite, Granite, Quartz, KREEP (Potassium, Rare Earth Elements and Phosphorus), and Basalt.
2. Second Generation: These are materials formed from bombardment of the surface, such as recrystallised rocks and impact breccias, which are fragments of rock produced in the heat generated by impacts.
3. Third Generation: These are the youngest class, and are formed from repeated micrometeorite bombardment of the surface. This bombardment breaks down rocks and rock fragments into powders which are then overturned and transported across the surface by further impacts, a process known as impact gardening, creating a top layer of fine-grained unconsolidated surface material, known as the regolith. This regolith covers almost all the surface, except for bedrock exposures, to an average depth of a few metres. Small impacts can also redistribute the regolith laterally across the surface without affecting the composition, changing the location of expected rock types and obscuring other minerals. Regolith breccias are examples of third generation materials, which are impact breccias that have been broken down and transported in this way.

Mixing of different ages and different precursor rock types forms a mineralogically-complex surface, but generalisations can be made. In terms of location, the lunar surface can be broadly separated into two groups, known as the maria and the highlands. The maria are composed of solidified basaltic lava flows found almost only on the near side, where lava flowed into craters and basins formed by large impacts. Therefore these rocks are younger than the surrounding highlands, and have a lower albedo due to their differing composition. The lunar highlands are mainly composed of older, anorthositic rocks, which have a higher albedo and therefore appear lighter than mare regions. This can easily be seen in images of the Moon seen from Earth, such as in Figure 1.

2.3 Surface Temperature

Daytime surface temperatures are governed by radiative equilibrium with the incident solar radiation, while night time temperatures are governed by thermal conduction from subsurface layers, as shown in Figure 2. Differences in thermal conduction between the regolith and rocks cause large temperature variations to be observed across the surface, as shown in some preliminary thermal model calculations in Figure 3. Rocks have a much higher thermal inertia than the regolith, which is the resistance of a material to changes in heating and cooling; analogous to how, in classical mechanics, an object's inertia affects its ability to resist changes of motion.

Thermal inertia is defined by the equation:

$$I = \sqrt{k \rho c} \qquad (1)$$

Where k is the material's bulk thermal conductivity, ρ is the material's density, and c is the material's specific heat capacity.

By observing the thermal emission from a given point on the surface across a range of local times of day, variations in radiance due to the rock to soil ratio can be identified separately from variations in radiance due to differences in rock and soil emissivity. Large- and small-scale surface roughness affect the temperatures measured, so both the reflectance and emission from the surface need to be determined.

2.3.1 Permanently Shaded Regions

The minimum temperature required for water ice to be permanently trapped is approximately ~112K; any greater than this and the thermal velocity of the molecules will be too great to remain retained by the Moon's gravity [Vasavada et al, 1999]. Water could also be destroyed by photo-dissociation of water molecules due to solar radiation or by collisions with particles from the solar wind.

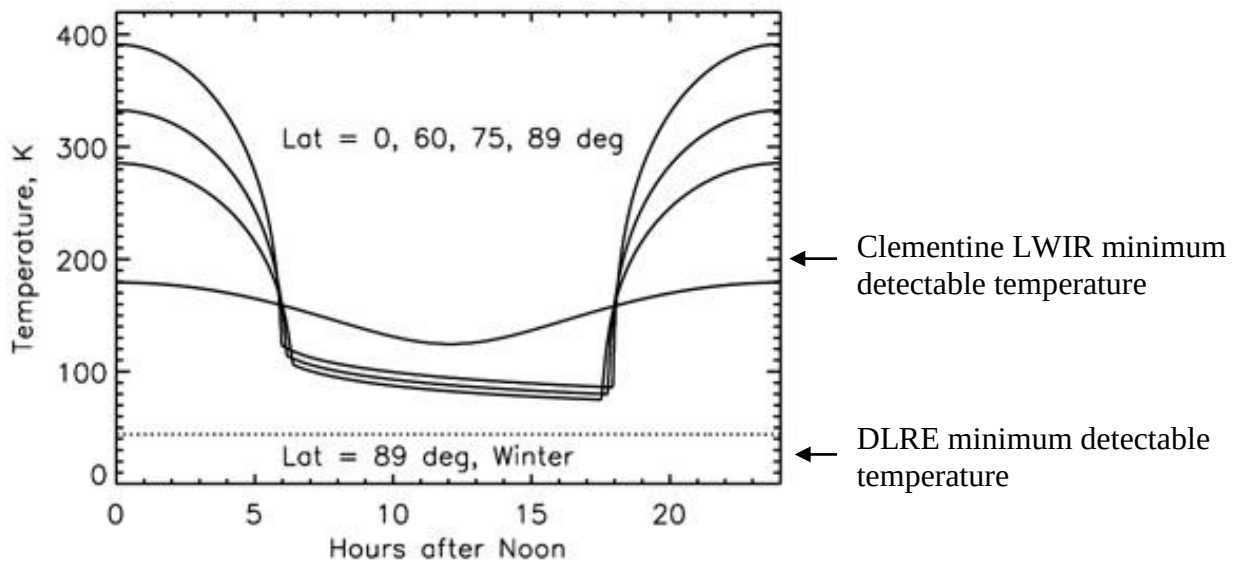

Figure 2: Model calculated diurnal lunar surface temperature variations over a complete diurnal cycle for horizontal surfaces at latitudes (from top to bottom) of 0◦, 60◦, 75◦, and 89◦ (summer) or 89◦(winter). The minimum detectable temperature of Clementine (section 3.1.2) and the DLRE instrument have been indicated [Chin et al, 2007].

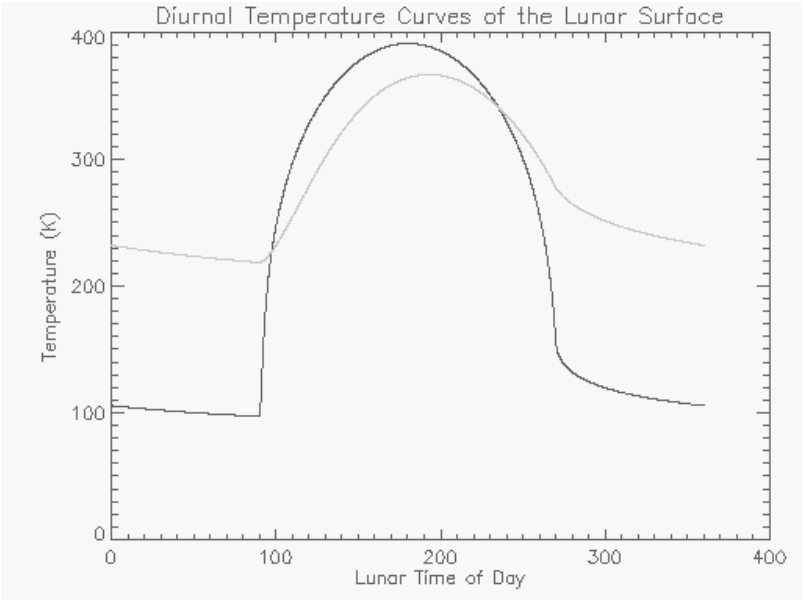

Figure 3: Modelled diurnal temperature curves for regolith (black) and rock (grey) in a mid latitude region, for a full lunar day (from 0 to 360°). The models were created using a 1-D Thermophysical Model written by John Spencer [Spencer, 1990]. Values used were: Albedo=0.123 (average bond albedo of the Moon), period=29.5 days (synodic period of the Moon), emissivity=0.9 (lunar average), thermal inertia=50 J m^{-2} K^{-1} $s^{-1/2}$ (regolith), 2400 J m^{-2} K^{-1} $s^{-1/2}$ (solid basalt) [Gaidos et al, 2006].

Assuming that the average geothermal heat from Moon's interior is ~2μW/cm^2 , as measured at the Apollo 15 and 17 landing sites [Heiken et al (eds.), 1991], and the average solar wind consists of ~2 x 10^8 particles/cm^2 with a typical energy of 3keV per particle, then the minimum energy of the surface at any point is ~2.1μW/cm^2. This corresponds to a minimum expected temperature observable on the moon of ~24K, far below the minimum retainable temperature for water molecules [Watson et al, 1961 & Arnold, 1979]. For a cold trap crater located at ~75° latitude, with a large 10° slope and large 1km^2 radiating area, then the expected temperature of the crater floor is only 94K, even with these large assumptions [Arnold, 1979]. Hence, provided that regions of the surface have been in permanent darkness for billions of years, there is a strong possibility that water ice could be present on or near the surface.

2.3.2 Permanently Illuminated Regions

A constant power source is an essential requirement for a permanent outpost to be established on the Moon, which is likely to be provided by solar cells. By mapping the surface temperature across many diurnal cycles, the regions in permanent sunlight can be found. Some areas of raised ground, such as crater rings and ridges, are expected to receive constant illumination, and are also located at the lunar poles.

2.4 Mineralogy

There are several methods for determining the surface mineralogy from orbit, by observing different regions of the electromagnetic spectrum. Gamma ray spectroscopy, as performed by the Lunar Prospector mission (section 3.1.3), can determine the presence of elements by measuring their radioactive decay (e.g. Thorium), though maps like these typically have a very low spatial resolution. Measuring surface spectra in the ultraviolet and visible ranges can map iron content; similarly infrared spectra can help to constrain silicate and iron-containing compound abundances. Pyroxene and olivine exhibit strong spectral features in the 1-2μm region due to electronic transitions in ferrous iron, though these optical properties can differ from laboratory measurements of the same rocks, due to space weathering effects [Pieters, 1993]. For example, the incident solar and cosmic radiation has been found to alter mineralogical structures in processes not observed on the Earth, such as reducing the iron in compounds to nanophase iron, which conceals predominant near-infrared spectral features, and depositing He^3 on the surface. The spectral properties of lunar soils also vary with grain size, which is one of the factors investigated in the project.

By mapping in the mid infrared region around 7-10μm, silicate structures such as pyroxene, feldspar and olivine, which are the most abundant minerals found in the crust, exhibit a spectral characteristic known as the Christiansen Feature. The Diviner instrument has the capability to measure in this spectral region, to map mineral abundances.

2.4.1 Christiansen Feature

The Christiansen Feature (CF) is a compositional indicator observed in spectra of the lunar surface. It is enhanced by the lunar environment, and is therefore the primary spectral feature in the mid infra-red (MIR), as shown from balloon-borne experiments in Figure 4.

This enhancement by the lunar environment comes from the large temperature gradient generated in the top of the surface. During the lunar daytime, the solar diurnal wave penetrates the top tens of centimetres of the surface. Due to the absence of an atmosphere, while this heating to depth is occurring, the top few microns of the surface are exposed to cold space, causing it to lose heat by radiation. The very low pressure prevents heat transport through the surface by convection, and the powdered nature of the regolith reduces heat transfer by conduction. These conditions produce a sharp thermal gradient in the top few layers, as described by thermophysical modelling in Figure 5.

Around the location of the CF in spectra, the surface becomes more transparent, and so the emission spectra show a peak where radiation from the hotter layers underneath can be observed. The effect of this can be measured in the lab by recreating the lunar surface environment, as has been performed previously in a similar way, but for a very limited number of samples [Logan and Hunt, 1970; Logan et al, 1973; Henderson et al, 1996].

Significantly, the spectral location of this transparency feature, and hence the location of the CF, varies between different minerals, and hence can be used to constrain surface composition, while being relatively unaffected by soil maturity effects. The lunar environment also reduces vibrational and restrahlen (strong reflection) bands, whilst causing this enhancement of the CF, making it a good compositional indicator [Greenhagen and Paige, 2006].

In reflectance measurements of minerals, the CF appears as a reflectance minimum, and hence as an emission maximum. The spectral location of this occurs near the Christiansen frequency, which is the location in frequency space where the refractive index of the soil approaches the refractive index of its surrounding medium, which for the lunar surface is the vacuum of space.

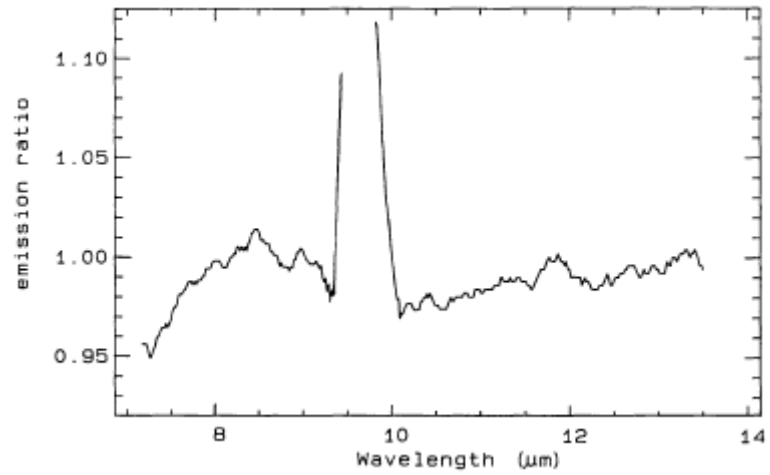

Figure 4: The ratio of the emission spectra of the central highlands/Copernicus of the Moon from Murcray et al, 1970, ratioed by Lucey, 1991. The measurements were made using a radiometer from 32km above the Earth's surface, minimising the effects of atmospheric absorption. The telescope used had a large field of view of 3 arcminutes, so the spectra observed are of entire regions of the Moon.

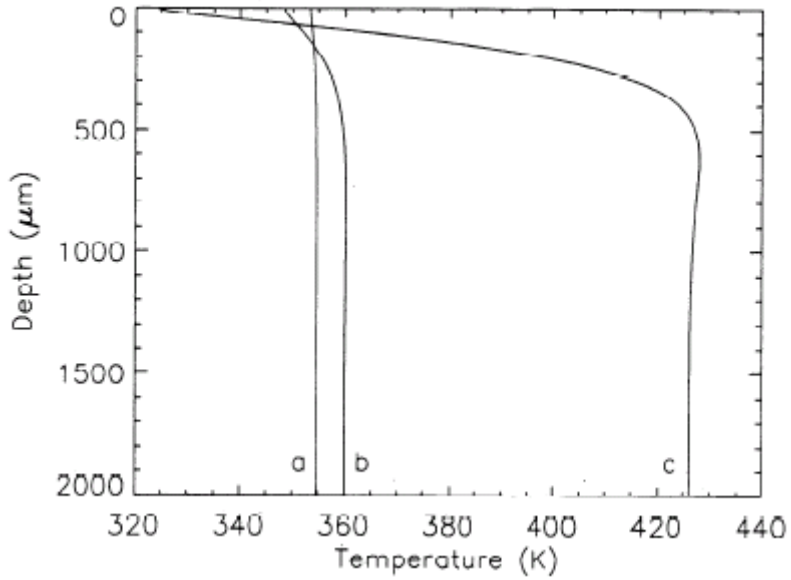

Figure 5: Thermophysical modelling of the thermal gradients observed in a quartz regolith, heated by sunlight normal to the surface, for three values of thermal conductivity [Henderson and Jakosky, 1997]. Curve c was made using a value for conductivity appropriate for lunar surface minerals, with a and b more akin to conditions on Earth and Mars.

3 Lunar Missions

3.1 Previous Missions

Since 1959, sixty-eight missions have been sent to the Moon, with varying objectives and degrees of success. Many of the early missions were technological demonstrations with minimal exploration objectives, or flybys before travelling further afield. The most notable exploration exercises were the manned NASA Apollo and unmanned USSR Luna missions, which returned lunar samples from various locations on the surface. These allow a correlation to be made between what is observed at these landing sites from orbit, and the actual samples taken from these locations, although only a limited number of sites have been sampled, all of which are located on the lunar nearside. In terms of relevance to the remote-sensing DLRE instrument, a few of the most important are outlined below.

3.1.1 Apollo 17, 1972

The Infrared Scanning Radiometer (ISR) onboard the Apollo 17 Command-Service Module was used to map the thermal emission of the lunar surface from orbit, but only consisted of a bolometer which could measure from 1.2 to 65μm [Mendell, 1974]. Whilst the temperature range of this radiometer was sufficiently large (85K-400K) to measure the diurnal temperature variations of most of the lunar surface, it was not capable of measuring the lowest temperatures of permanently shaded craters. The spatial resolution of the instrument was also relatively large, at 2.2km, impairing detection of smaller scale features.

The whole surface would be expected to heat and cool in a regular repetition, governed by the diurnal cycle of the slowly rotating Moon. While these diurnal temperature variations were viewed, thermal anomalies were also observed in some locations, where the surface would cool down more slowly than surrounding areas when solar illumination ceased. These thermal anomalies were found to occur in locations containing surface rocks, due to the higher thermal inertia of the rocks slowing their rate of cooling compared to the regolith.

The number of rocks exposed in an area depends on many factors, such as age (as all rocks are eventually comminuted to soil by impacts) and on processes which expose and cover rocks, such as mass-wasting, slumping and avalanching. Hence from the ISR measurements alone, constraints can be placed on these surface evolution processes [Mendell, 1974].

3.1.2 Clementine, 1994

The Clementine Orbiter contained a Long-Wavelength Infrared (LWIR) camera, which mapped 0.4% of the night-time surface of the Moon at a resolution of 55-136m per pixel, before the spacecraft malfunctioned [Nozette et al, 1994]. The minimum detectable temperature of this camera was approximately 200K though, so no permanently shaded regions or night-time regolith temperatures could be adequately thermally mapped. Another onboard camera mapped the surface in the ultraviolet-visible region of the spectrum, using five channels between 0.4 and 1.0μm, with a resolution of 100-300m [Tompkins and Pieters, 1999]. From these measurements, mafic minerals (rich in magnesium and iron, such as olivine and pyroxene) were identified from orbit, due to the minerals having absorption bands in their reflectance spectra around these wavelengths. Regolith abundances of FeO and TiO_2 have also been determined from the UV-VIS camera data.

The Clementine Bistatic Radar Experiment was an extra experiment performed at the end of the Clementine mission. It measured the magnitude and polarisation of the radar echo from the lunar surface versus the bistatic angle (angle between transmitter and receiver), using the Deep Space Network of receivers on Earth to observe radiation scattered from the surface from the onboard transmitter [Nozette et al, 1996]. The results showed that echoes from permanently shadowed regions near the south pole exhibited an enhancement compared to other areas of the surface periodically exposed to solar illumination. From these results it was inferred that low-loss volume scattering substances, such as water ice, could be present in these regions of permanent shadow. Even though no equivalent enhancements were found at the north pole, contrary to expectations, this discovery was enough to warrant another mission with a more specific instrument suite, the Lunar Prospector.

3.1.3 Lunar Prospector, 1998

The Lunar Prospector was a lunar orbiter, launched in 1998, which contained a neutron spectrometer designed to continue the investigation into possible water ice abundances. Epithermal neutron data, measured by the Lunar Prospector Neutron Spectrometer, was studied to estimate the magnitude of potential water ice deposits [Feldman et al, 1998]. Several large polar craters were observed at the south pole, along with polar plains contain many small craters at the north pole, all of which contain regions residing in permanent shadow. An increase in Hydrogen concentration, [H], was observed in these craters, suggesting that the temperature (and hence rate of sublimation of water) of the lunar surface is the factor discriminating regions of enhanced [H] from those that do not. For the south pole, it was estimated that [H] = 1700±900ppm, which equates to a water concentration of $[H_2O] = 1.5 \pm 0.8\%$, while for the north this was estimated at >10%, though this estimate is very uncertain. The results are shown in Figure 7.

The Lunar Prospector Gamma-ray Spectrometer measured the energy and flux of incident gamma rays with 150km surface resolution, allowing elemental analysis of the surface to be conducted [Lawrence et al 1998]. The instrument produced global maps of the elements uranium (U), thorium (Th), potassium (K), iron (Fe), titanium (Ti), oxygen (O), silicon (Si), aluminium (Al), magnesium (Mg), and calcium (Ca), which either emit gamma rays through spontaneous decay processes, or when impacted by the solar wind or cosmic rays.

The Lunar Prospector mission ended when it was intentionally crashed into a permanent shaded crater at the lunar south pole, while Earth-based observatories monitored the crash site for evidence of water in the debris plume. No water ice was detected, but this could be explained if: the spacecraft missed the target area or hit a rock or dry soil at the target site; the water molecules are firmly bound in rocks as hydrated mineral as opposed to existing as free ice crystals, with the crash lacking enough energy to separate water from hydrated minerals; studies of the impact's physical outcome were inadequate; the parameters used to model the plume that resulted from the impact were inappropriate; the telescopes used to observe the crash, which have a very small field of view, were not pointed correctly; water and other materials did not rise above the crater wall or otherwise were directed away from the telescopes' view [Isbell, Morse & Rische, press release 1999]. With all these uncertainties, the question of whether water ice exists on the Moon could still not be answered for definite.

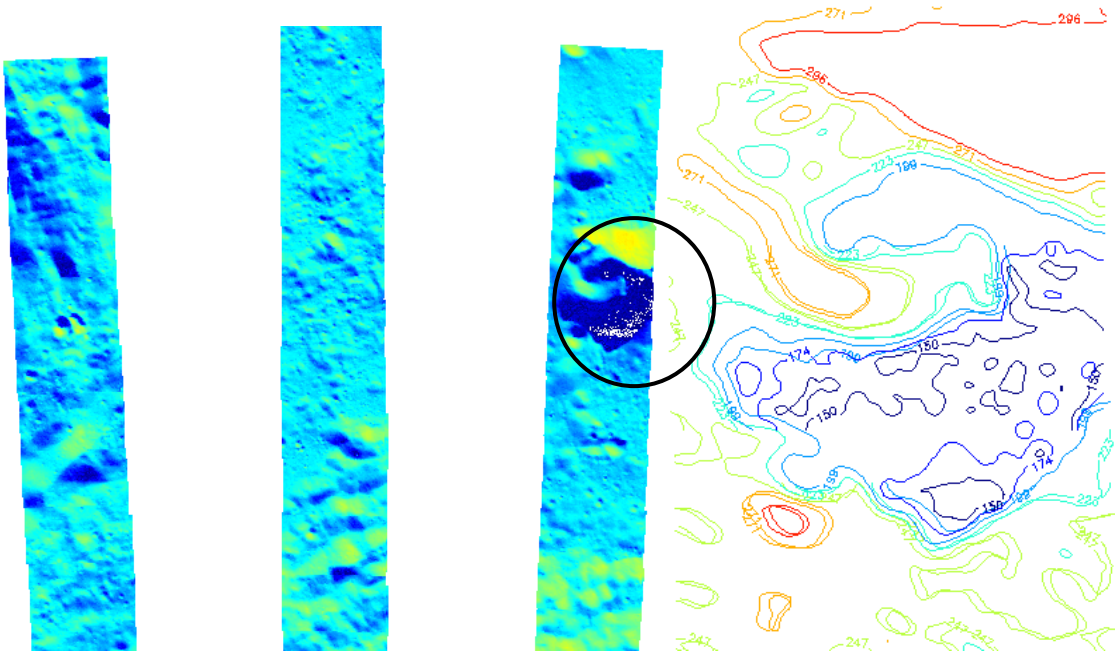

Figure 6: Clementine LWIR temperature data, showing gaps in coverage (left) and an enlarged view of a crater showing temperature variations of the surface, generated in IDL (right). The minimum detectable temperature of the instrument was ~200K for adequate signal to noise, and so the crater floor could not be mapped reliably. Differences in temperatures can be clearly observed.

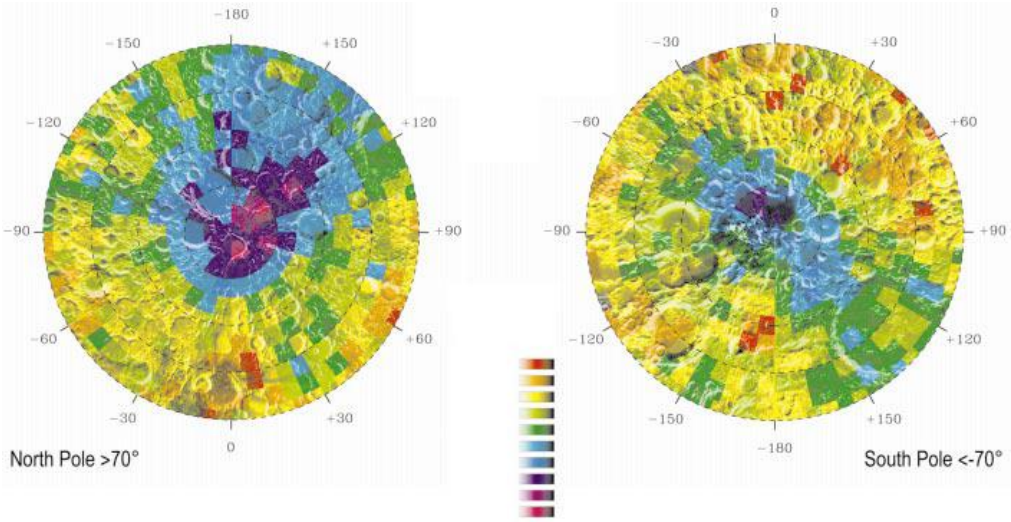

Figure 7: Epithermal neutron count rate for both lunar poles, showing increased hydrogen detected at the north and south poles, with craters superimposed on the maps [Feldmann, 1998].

3.1.4 SMART-1, 2003

The Small Missions for Advanced Research in Technology (SMART-1) lunar orbiter incorporated the Demonstration of a Compact X-ray Spectrometer (D-CIXS), the SMART-1 Infrared Spectrometer (SIR) and the Advanced Moon Imaging Experiment (AMIE) instruments, which were all capable of mapping lunar mineralogical abundances [Foing et al, 2006]. D-CIXS compiled an X-ray map of Magnesium (Mg), Aluminium (Al) and Silicon (Si) with 50 km resolution. The SIR was the first instrument to map mineralogy using 256 spectral channels in the region 0.9–2.5μm, while the AMIE mapped at 0.75, 0.9 and 0.96 μm. The instruments also discovered a hill on a ridge to the southwest of Shackleton crater at the south pole that is constantly illuminated during the lunar southern summer, which could be a potential location for a manned outpost [Sanderson, 2007].

3.1.5 SELENE, 2007

The Terrain Camera (TC) on the Japanese Space Agency's SELenological and ENgineering Explorer (SELENE) was able to image Shackleton Crater, a permanently shaded crater near the lunar south pole, as shown in Figure 8. No sunlight can directly reach the crater floor, but light scattered from the inner crater wall allowed the image to be taken. From simulations based on the new data, they were able to infer that the maximum temperature of the crater floor should be around ~88K close to this central peak.

Also, the laser altimeter onboard SELENE mapped a high resolution, global topographic map similar to what the LOLA instrument is currently measuring, and so will be a very useful backup in case of a fault with LOLA.

3.1.6 Current Missions

Chandrayaan-1, a satellite from the Indian Space Research Organization, and Chang'e 1, from the China National Space Administration, are currently orbiting the Moon along with LRO. Some results were released from the Moon Mineralogy Mapper (known as M^3), a near infrared hyperspectral imager, as shown in Figure 9. More results are expected to be announced in future from both Chandrayaan-1 and Chang'e 1.

3.1.7 Ground Based Instruments

The Arecibo Observatory Planetary Radar in Puerto Rico was used to map areas of the lunar poles visible from the Earth [Campbell et al, 2003]. Radar measurements showed that permanently shaded areas did not give rise to strong backscattering or the distinctive polarisation signatures associated with thick ice deposits. Any lunar ice present within the regions measureable by the Arecibo dish must therefore be in the form of distributed grains or thin layers, or be buried under several metres of dust, where the 70cm wavelength radar cannot probe. The radar echo from the floors of craters Hermite and Peary near the north pole, and Shoemaker and Faustini near the south pole, showed no difference in radar-scattering from the lunar highlands. The floor of Shackleton crater, where Clementine bistatic radar images inferred the presence of thick ice deposits, cannot be viewed from the Arecibo dish; while the Lunar Prospector observations can be attributed to thin ice deposits; leaving the presence of the water ice still unsubstantiated.

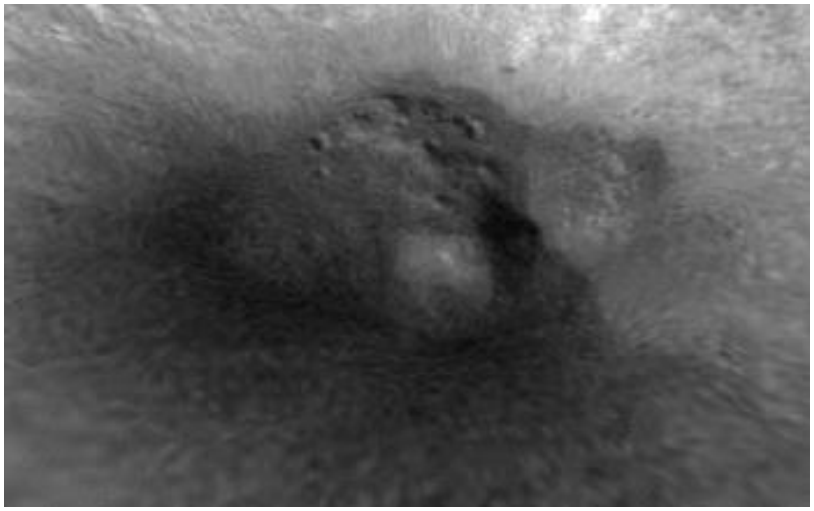

Figure 8: An image of central peak of Shackleton Crater, taken by the Terrain Camera on SELENE [Haruyama et al, 2008]

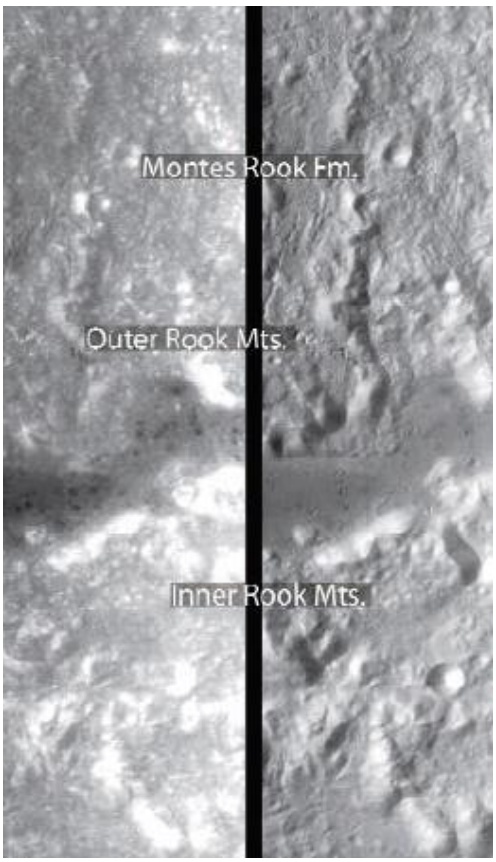

Figure 9: Early results from the Moon Mineralogy Mapper onboard Chandrayaan-1 [Kerr (ed.), 2009]. The bright areas indicate regions of nearly pure plagioclase.

3.2 The Lunar Reconnaissance Orbiter

A computer generated image of the spacecraft is shown in Figure 10.

3.2.1 Mission Objectives

The LRO spacecraft is currently in a commissioning orbit, where all the instruments are switched on and checked. This orbit is elliptical, with a swath width much greater at the north pole than the south pole. Once LRO has been inserted into its correct orbit, which is currently due to occur on 15th September 2009, the mapping phase of the mission will begin. The satellite will be placed in a very low orbit, just 50km from the average surface, in order to achieve high resolution mapping. The orbit plane will be almost fixed in inertial space (relative to the stars) with an inclination (the angle between orbital plane and plane of lunar spin) of approximately 90°, therefore the sub-spacecraft longitude will cycle from 0° to 360° once per Earth month. This will give good coverage of the whole surface, with the opportunity to view a given point on the surface at a given local time twice per year [Paige et al, 2009].

3.2.2 Overview of Other Onboard Instruments

A brief description of the other instruments onboard the LRO satellite is given below [Chin et al, 2007]:

The Lunar Orbiter Laser Altimeter (LOLA) is a Light Detection and Ranging (LIDAR) system used to measure the topography of the whole lunar surface with 10cm vertical and 25m horizontal resolution. It will be essential for combining crater topography and surface roughness with Diviner temperature measurements in the thermophysical model (section 7).

The Lunar Reconnaissance Orbiter Camera (LROC) will photograph the surface to characterize polar illumination conditions and to identify potential resources, and also take narrow angle images of the lunar surface, allowing metre-scale features to be resolved to support landing site selection. Data can be used to compare inferred rock abundances to visible surface rock densities, and can also detect Ilmenite due to its multispectral imaging capability.

The Lunar Exploration Neutron Detector (LEND) will map the flux of neutrons from the lunar surface with a resolution of 10km, to search for evidence of water ice, and will provide space radiation environment measurements that may be useful for future human exploration. It will map Hydrogen concentrations, with a sensitivity of up to 100ppm at the poles, to characterise surface distribution and density of possible water ice deposits in the Moon's permanently shaded regions, the locations of which can be identified and compared with locations of these regions determined by Diviner.

The Lyman-Alpha Mapping Project (LAMP) will map the entire lunar surface in the far ultraviolet. LAMP will search for exposed surface ice and frost in the polar regions and provide images of permanently shadowed regions illuminated only by starlight, by mapping all permanently shadowed regions to 100m resolution. As with LEND, locations of detected water by LAMP can be compared to locations of permanently shaded regions found by Diviner.

Figure 10: A computer generated model of LRO orbiting the Moon, with Diviner indicated by the white arrow.

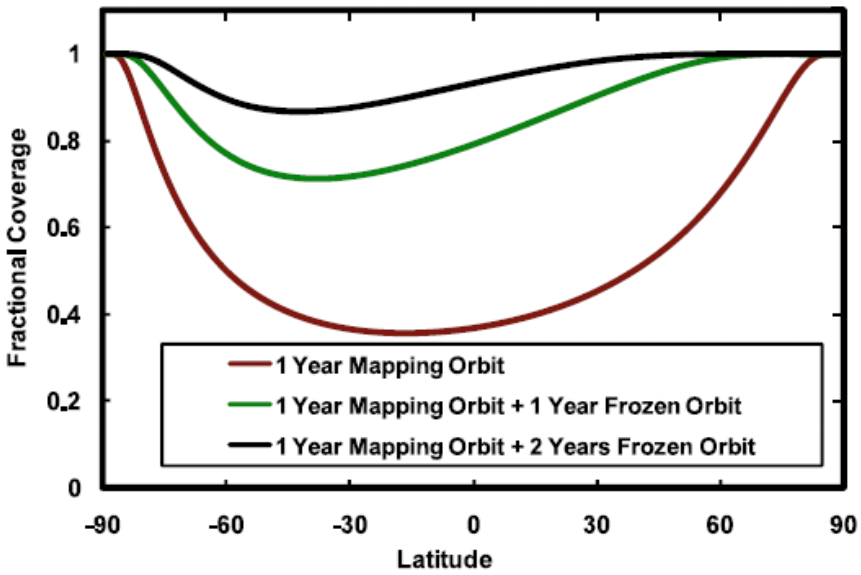

Figure 11: The fraction of the lunar surface which will be mapped each year around noon-time, plotted as a function of the Moon's latitude [Paige et al, 2009].

The Cosmic Ray Telescope for the Effects of Radiation (CRaTER) will investigate the effect of galactic cosmic rays on tissue-equivalent plastics as a constraint on models of biological response to background space radiation.

Also being launched simultaneously with LRO will be the Lunar Crater Observation and Sensing Satellite (LCROSS). LCROSS will separate from LRO and enter an elliptical orbit, eventually ending in the spacecraft colliding with the surface. It will be preceded in impacting by the upper stage of the rocket, which will hit a permanently shaded crater, throwing up debris above the lunar surface. The LCROSS craft, which contains three spectrometers, five cameras and a radiometer, will then pass through this debris plume four minutes later, analysing its constituents. The debris plumes are also expected to be visible from telescopes on and above the Earth.

4 Diviner Lunar Radiometer Experiment

4.1 Design

Diviner is a near build-to-print copy of Mars Climate Sounder, a filter radiometer currently orbiting Mars onboard the Mars Reconnaissance Orbiter spacecraft [McCleese et al, 2007]. It was originally designed for temperature mapping and detection of surface and sub-surface water, but the water detection channels have since been replaced by channels dedicated to observing the Christiansen Feature of surface minerals, as the water detection channels would have had an insufficient signal to noise ratio when mapping the very cold permanently shadowed regions.

The design, as shown in Figure 12, is mounted near the underside of the LRO satellite, and features azimuth and elevation actuators, allowing the telescopes to be pointed in any direction. Typically, they will usually be pointed downwards for nadir viewing, but can alternatively be pointed at an angle towards any point on the viewable surface in order to record emission with varying phase angles.

For in-flight calibration purposes, a solar calibration target and two accurate blackbody targets are also incorporated into the design, which are viewed periodically to provide one calibration reference point. Pointing the telescopes into cold space provides the other reference point. The solar calibration target also gives the local solar irradiance, which is essential for determining the albedo of the surface, from which the radiative balance can be determined.

4.2 Goals of the DLRE

The goals of Diviner can be summarised as follows [Paige et al, 2009]:

1. To characterise the Moon's surface thermal environments:
    a. Daytime
    b. Night-time
    c. Polar
2. Map properties of the lunar surface:
    a. Bulk thermal properties
    b. Rock abundance
    c. Mineralogy
3. Characterise polar cold traps:
    a. Map cold trap locations
    b. Determine their physical properties
    c. Assess potential lunar water ice resources

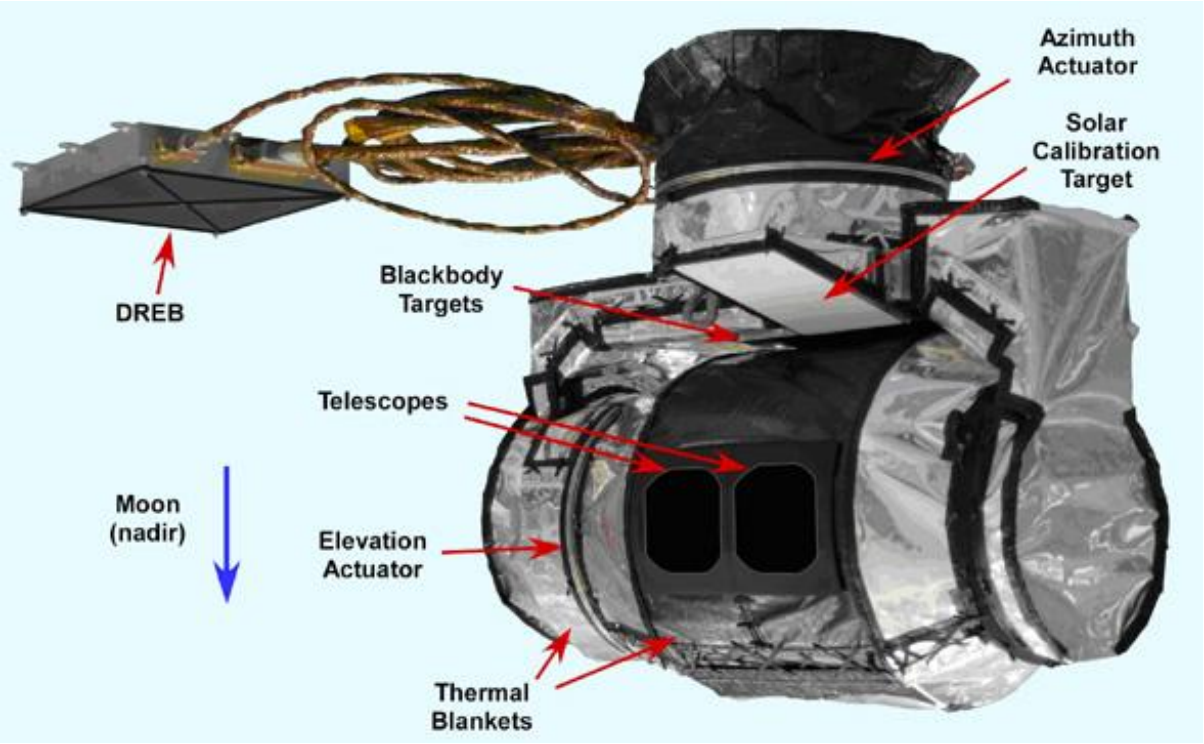

Figure 12: A diagram of the Diviner instrument. The instrument is positioned close to the underside of the spacecraft; hence the image has been flipped to show its true orientation with respect to the lunar surface.

4.3 Diviner Spectral Channels

The Diviner instrument contains nine channels (Table 1). The filter responses, with relation to ideal blackbody curves, are shown in Figure 13.

The A1 and A2 channels measure solar reflectance from the surface. A1 is sensitive to determine the solar reflectance in permanently shadowed regions, while A2 will measure the reflectance from sunlit regions. A3-A5 have narrow bandpasses centred around the spectral location of the Christiansen Feature, allowing variations in surface composition to be found from the measured thermal spectra. Channels A6-B3 will be used to accurately calculate the temperature of the surface from thermal emission, and will be able to determine rock abundances from measurements of surface cooling rates. The selective transmissions of each channel are achieved by using filters which are secured in filter assemblies located 100μm from an array of uncooled thermopile detectors. To achieve high mapping resolution, each of the nine thermopile arrays contain twenty-one individual detectors, which when viewed in cross-track scanning mode results in a surface field of view of 160m per detector [Paige et al, 2009].

Parylene-coated KCl blockers have been added in front of the A1 and A2 filters to block long-wavelength leaks outside of the intended bandpass, and similarly Quartz windows have been added to the B2 and B3 filters to block short-wavelength leaks. A specially designed multilayer filter has been placed in front of the B1 filter also, in order to stop these short-wavelength leaks, which are inherent to all mesh filters.

These blockers and windows are required to avoid unwanted effects, such as those present in the Mars Climate Sounder (MCS) instrument. In MCS, before integration into the instrument, the B1-B3 channels met their specifications, but the spectral response had changed during pre-flight testing [McCleese et al, 2007]; although on-going further investigations hint that this may have been due to unforeseen spectral leaks in the monochromator used to make the measurements [Lolachi and Bowles, personal communication 2009]. To reduce unwanted effects, baffles have been incorporated into the optical assembly to minimise scattering within filters and emission from detectors.

The focal plane assemblies in the Diviner instrument were manufactured and assembled by the Atmospheric, Oceanic and Planetary Physics Group in Oxford. The B1-B3 mesh filters were supplied by the Astronomy Instrumentation Group at Cardiff University, and the Infrared Multilayer Laboratory at the University of Reading supplied the other filters, KCl blockers and Quartz windows.

Telescope number	Channel number	Bandpass (μm)	Function
A1	1	0.35–2.8	High Sensitivity Solar
A2	2	0.35–2.8	Mid Sensitivity Solar
A3	3	7.55–8.05	Mineralogy
A4	4	8.10–8.40	Mineralogy
A5	5	8.38–8.68	Mineralogy
A6	6	13–23	Thermal
B1	7	25–41	Thermal
B2	8	50-100	Thermal
B3	9	100-400	Thermal

Table 1: Properties of Diviner's Spectral Channels [Paige et al, 2009].

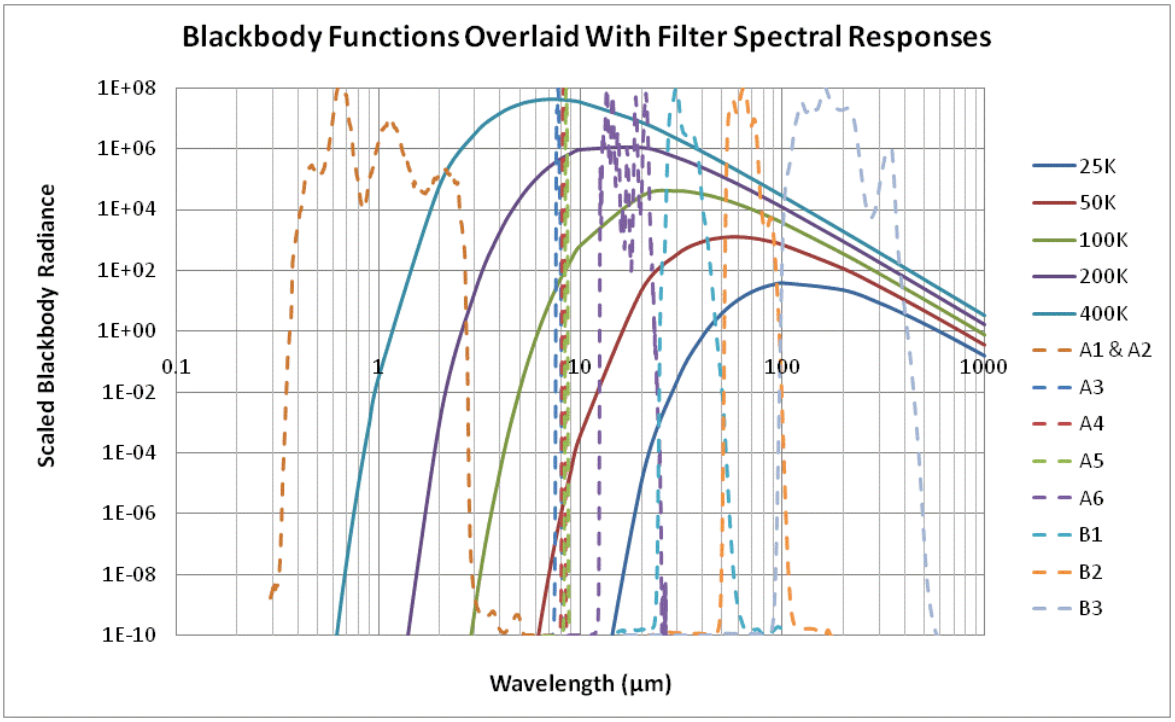

Figure 13: A plot showing the blackbody functions of various temperatures, overlaid with the normalised DLRE filter responses.

5 Filter Measurements

Due to the problems experienced with the changing filter profiles in the MCS instrument, and the fact that Diviner uses the same design, it was essential to accurately characterise the instrument's filters, in addition to the extra blockers and filters used to try to reduce the effects seen in MCS. Therefore, a significant component of this project has involved characterisation of several instrument filters that had not been previously determined, as well as confirming previously measured results. Specifically, this has involved:

- Measuring the spectral response of the Parylene-coated Potassium Chloride (KCl) blockers used on the A1 and A2 channels,
- Completing the B2 and B3 channel stack and individual measurements,
- Determining if there were any changes in the spectral responses of the B1-3 filters when measured at a short distance from the detector, as they are in the instrument.

Accurate measurements of the filters are essential for calibration and determination of the location of the Christiansen Feature, which due to time constraints at the calibration test facility, could not be performed using the Diviner flight model, and so had to be performed in the laboratory.

5.1.1 B2 and B3 Filter Measurements

The B1-3 filters used are each composed of three meshes with carefully chosen spectral transmissions, so that when combined they produce the desired spectral response, as shown in Figure 15. The overall stack transmissions can, in theory, be found by multiplying the spectra of the individual meshes together, but this needed confirmation. The B1 filter had already been measured as a stack, but the B2 and B3 filters had only been measured as individual meshes at Cardiff University, and not as a combined stack as in the instrument. Therefore, the transmissions of the combined stacks were found, to ensure that the overall spectral responses agreed with what was expected.

The measurements were made in a Brüker IFS 66v Fourier Transform Spectrometer at AOPP, using the Mylar beamsplitter combined with Globar^{TM} source and FIR DTGS detector. Three measurements were taken per filter and averaged, each consisting of 500 scans with a 5mm aperture, 1.6kHz scanner velocity and 4x gain. Two background spectra were taken without the filter present, each consisting of 200 scans co-added together. The filter transmissions were found by dividing the averaged filter measurement by the averaged background measurement, the resulting spectra of which are shown in Figure 14.

5.2 Short-distance Filter Measurements

One of the uncertainties found in the Mars Climate Sounder instrument was that the close proximity of the detectors to the filters, combined with the steep incident cone angle of the f/1.7 beam incident upon the filters, was thought to have caused the mesh filters to exhibit a different spectral response from those measured before the filters were integrated into the MCS instrument. This effect primarily manifested itself as a significantly broadened filter response with an increased full-width-half-maximum.

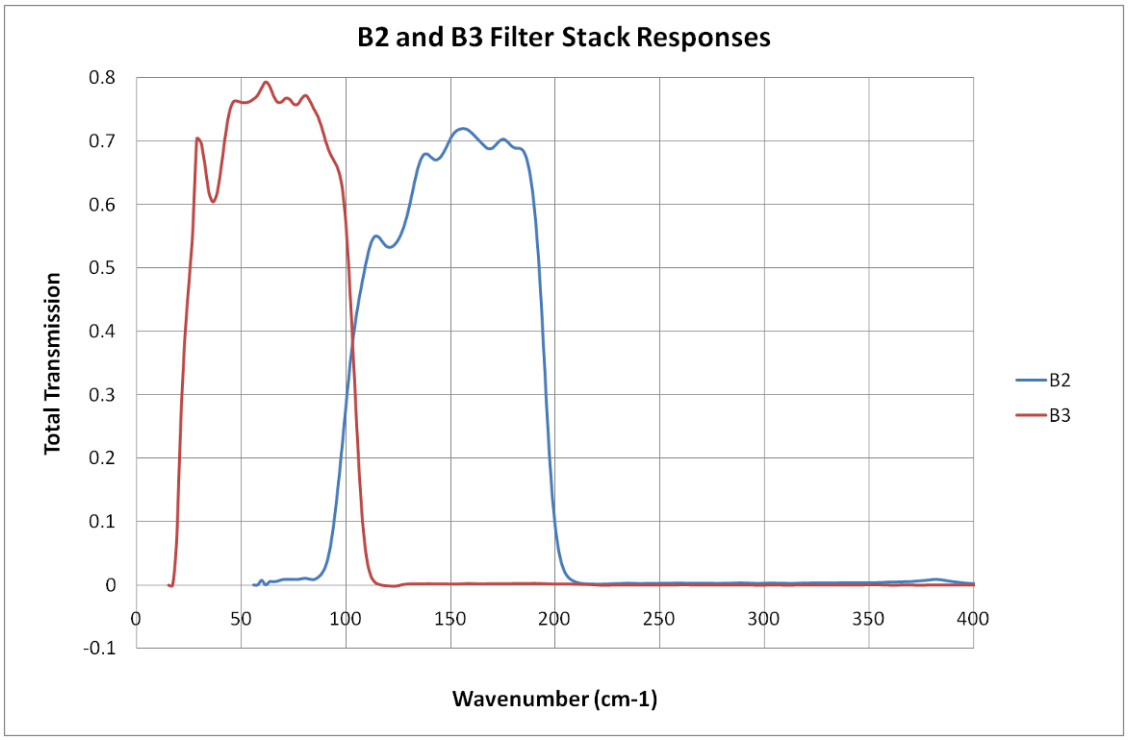

Figure 14: Transmission spectrum of B2 and B3 mesh filters. Due to limitations of the Brüker FTS at small wavenumbers, the lower cut-off of the B3 filter may slightly vary in shape from the recorded spectra. These filters were measured in early 2008, prior to the radiometric calibration analysis.

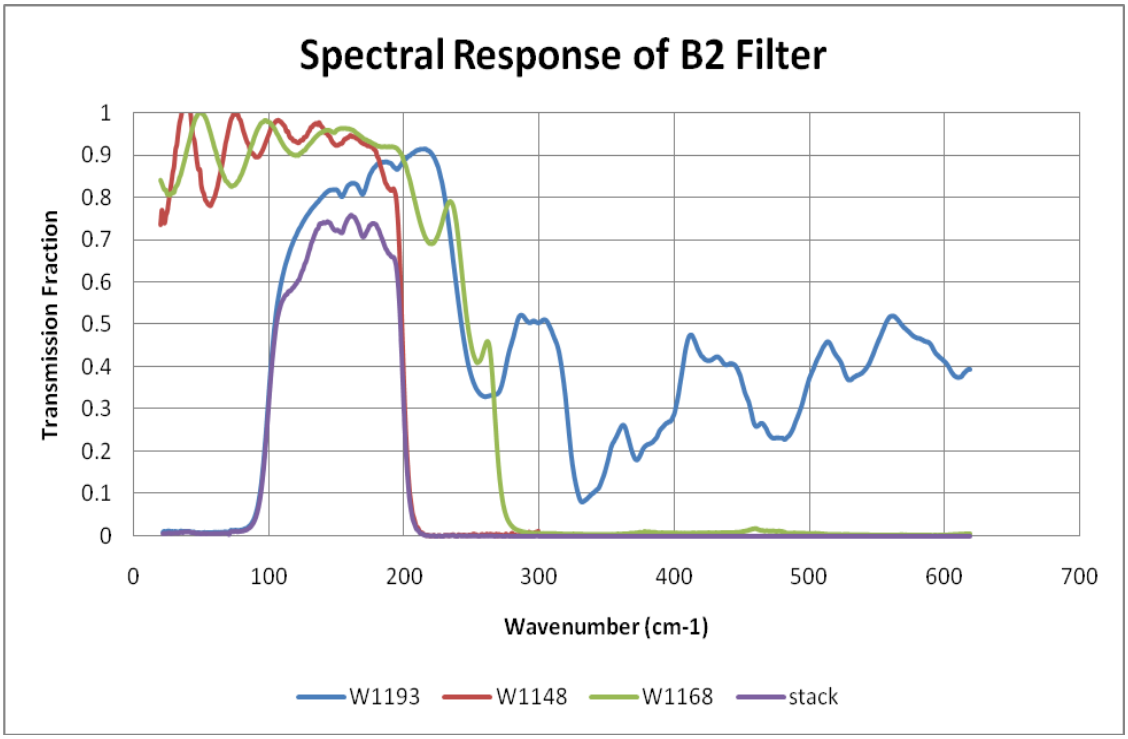

Figure 15: Spectral response of each of the individual meshes comprising the B2 filter, as measured by the University of Cardiff, and the total transmission of the stack, measured in the Brüker IFS 66v at Oxford.

5.2.1 Filter Holder

In order to recreate the optical setup inside the Diviner instrument as closely as possible, a filter holder was constructed which allows the distance from filter to detector to be varied from 1cm to 100μm in precise steps. A diagram of the filter holder is shown in Figure 16.

The optical setup used for the measurements involved placing an off-axis paraboloid in the sample compartment, so that the beam focuses down at a right angle to the incident beam, with the detector at the focus. As the beam in the sample compartment is converging with focal ratio f/3.8, an elliptical mirror would be required to form a perfect f/1.7 beam, but these bespoke mirrors are expensive and so an off-axis paraboloid (OAP) was used instead. This produced a beam with a convergence of approximately f/1.4, to a spot size of less than the width of the detector. Therefore, if there is an effect owing to the beam shape, which is the aim of the measurements, the effect will be amplified by using a sharper convergence angle.

5.2.2 Choice of Detector

In order for the detector to be placed as close as 100μm from the filter, the detectors already installed in the spectrometer could not be used, as they were all canned. A can is a built-in housing with filter window placed around the detector element that prolongs the life of the detector but can reduce the spectral range of the detector (depending on the window) and prevents anything from getting to within a few millimetres of the detector element. Therefore, in order to measure at such short distances across a wide spectral range, it was essential to find a suitable detector and to remove the can. Another requirement, for use in the Brüker IFS 66v, was that the detector must have a sufficiently short time constant in order for the interferogram to be recorded accurately, ruling out the use of thermopiles as used in the actual Diviner instrument.

Three detectors were tested: an Infratec LIE-332f, an Infratec LIE-502 and an Infratec LIE-312f. The latter two were already on loan from Surrey Satellites Technology Limited (SSTL), and came with the can already removed and with detector pre-amplifier electronics included. The LIE-332f was carefully de-canned on a lathe and a suitable pre-amplification circuit (section 5.2.3) was designed and produced to allow the detector to be connected to the Brüker FTS.

Initially, the default Brüker detectors (which are assumed to have uniform response over their given spectral range) were measured with various beamsplitters in order to distinguish whether low responsivity in several spectral locations was due to the transmission properties of the beamsplitter or due to the response of the detectors being tested. Then the Infratec detectors were measured and compared to the default Brüker detectors, to check that they had an adequate response across the spectrum. The scanner velocity was also varied to determine which detector worked at the higher scanner mirror speeds, and therefore took the least amount of time to record a scan.

The LIE-502 was found to only function well at low mirror scanner velocities, and so was discounted. It was found that the LIE-332f and LIE-312f performed very similarly, so the LIE-332f was used, as the pre-amplification circuit had already been made.

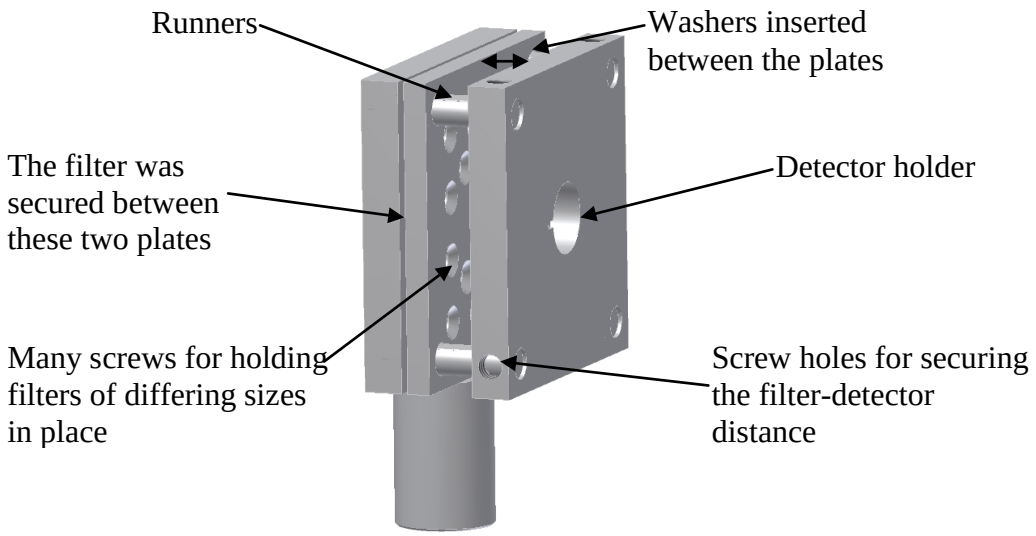

Figure 16: Autodesk® Inventor™ CAD drawing of the short-distance filter holder. The detector was attached to the right-hand plate, which was kept at the focus of the spectrometer beam. The filter was held between the two plates on the left, which could move on the four runners in each corner to vary the filter-detector distance. In order to keep the filter and detector holders at the required distance apart, washers of specific widths were made to fit between the plates, with a screw inserted into the hole in each corner to secure the filter holder. Adhesive Poron™, a compliant plastic, was stuck to the left-most plate to prevent the metal holder from damaging the filter. The filters were cut into various sizes, therefore many holes were required in the filter holder plates to ensure they were held securely.

5.2.3 Detector Electronics

The Infratec LIE-332f detector required a power supply and pre-amplification of output signal for integration into the Brüker FTS. Before the can was removed from the LIE-332f-16, an initial circuit was prototyped. The bias voltage supply circuit for the detector was taken from the Infratec detector datasheet, and the amplification and high pass filter were based on the circuit supplied by Brüker for their own detectors. The high pass filter reduces low frequency noise from the recorded interferogram. Initial spectra recorded using this circuit exhibited large periodic spikes, which were attributed to a combination of 50Hz mains noise and to pick-up in the secondary gain circuit inside the spectrometer itself. This spectrometer gain circuit is a computer-controlled amplifier, amplifying the voltage from the detector circuit before processing the signal and calculating the Fourier transform. This problem was solved by adding a voltage regulator to the circuit and by switching off the spectrometer internal gain circuit, thereby decreasing the signal level of the measured spectra but removing the spikes. The final circuit design is shown in Figure 17.

5.2.4 Accurately Determining the Detector to Filter Distance

A coordinate measuring machine (CMM) was used to determine the relative distance between the front of the detector element and the plate onto which the detector is mounted. The detector element was found to be sufficiently flat, at an angle of 0.67±0.05 degrees (Figure 18) to the plate, which equates to an error of 23±2 microns across the width of the detector.

These measurements made on the CMM were then used to determine washer widths (Figure 16) required to keep the detector at set required distances from the filter.

The distance between the detector and the plate where the filter is attached was found to be -1090 microns (i.e. if no washer is present, the detector element would protrude this distance through the filter). Therefore, for filter to detector distances of 50, 100, 200, 500 and 1000 microns, washers of widths 1140, 1190, 1290, 1590 and 2090 microns were required. These were made by machining mild steel washers to within +100 microns of these tolerances, and then grinding down to within ±10 microns of their required width using a surface grinder. The uncertainty in the plate width was ±10 microns, giving a combined uncertainty, by adding in quadrature, of $(23^2 + 10^2 + 10^2)^{1/2} = 27$ microns.

5.2.5 Measurement Procedure

The OAP and filter holder jig, without filter, were aligned correctly by switching to the quartz-halogen source (visible) in the spectrometer and manually adjusting the distance to find the focus of the beam. The source was then switched to the Globar™ and aligned by maximising the interferogram signal on the detector. Background readings (without a filter present) were taken between all filter measurements, with every washer size. The 50 micron washer was not used, as the detector had a small gold wire embedded into the element, which was in danger of touching the filter at such a short distance away. Before carefully mounting the filter stacks in the correct order, the holder was washed with acetone and left to dry, to keep the filters pristine.

The main cause of differences between measurements was from the jig not being in exactly the same position each time, which did not affect the spectral shape measured, but occasionally caused the amplitudes of spectra to vary by up to 10%. To prevent this from affecting the final filter responses, every spectrum taken was normalised, as the aim of the experiment is to determine if the width of the filter bandpass varies with filter-detector distance.

The spectra were taken with the Mylar beamsplitter and Globar™ source, with a 5mm aperture and mirror velocity of 1.6kHz. The number of scans varied between filters: B1 had a high signal throughput, and so only 100 scans were needed, whereas 200 were averaged together for B2, and 400 for the B3 filter. 50 scans were used for the background measurements. Each filter was measured three times per washer, normalised and each of these three measurements were averaged. The filter transmission for each washer was then found by dividing the averaged normalised filter response by the average normalised background for that specific washer. The result was then re-normalised to show a maximum transmission of 1 to allow comparison between filter-detector distances. The results are shown in Figure 19, Figure 20 and Figure 21, with the 1190 micron washer corresponding to a detector-filter distance of 100 microns, 1290 to 200 microns, 1590 to 500 microns, and 2090 to 1000 microns.

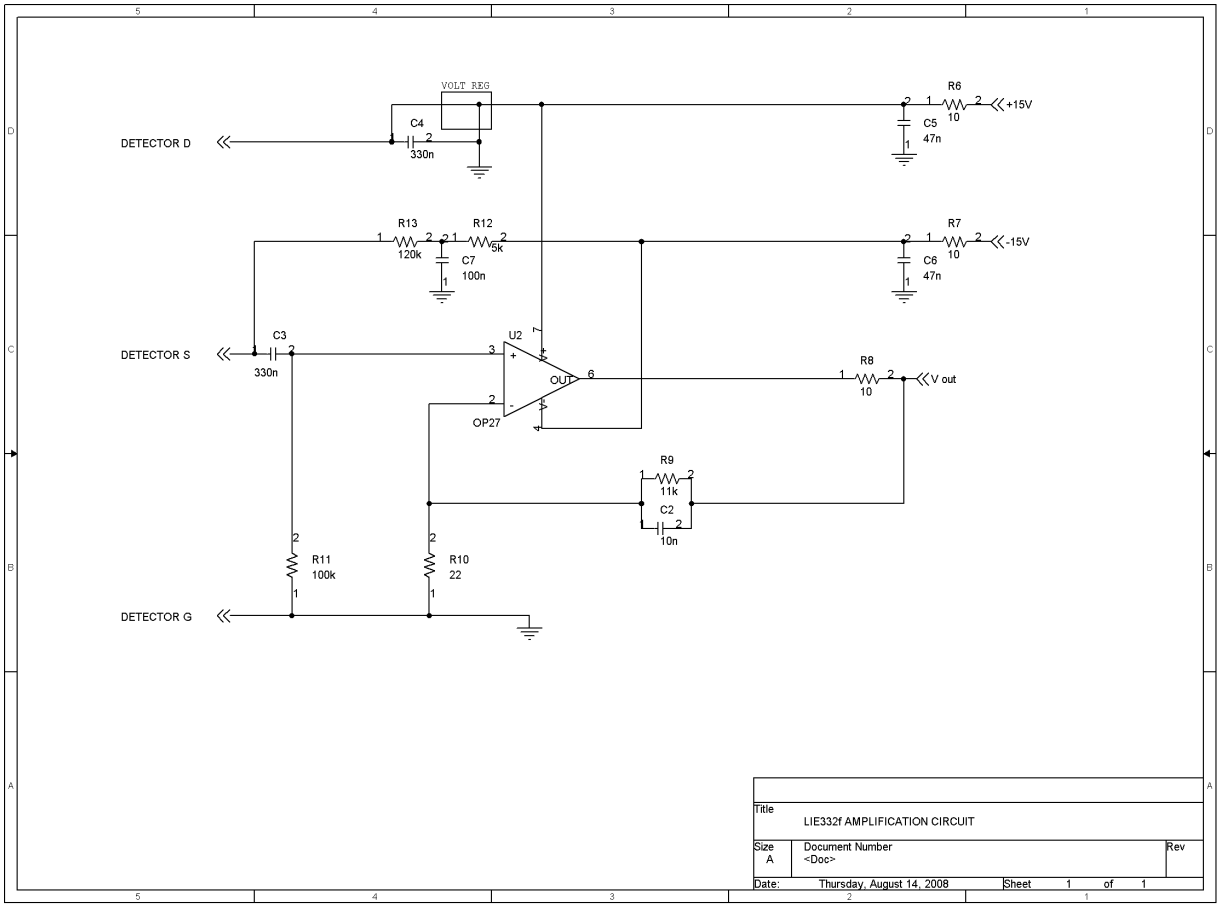

Figure 17: A Cadence® OrCAD™ diagram of the pre-amplification circuit constructed for the LIE-332f detector.

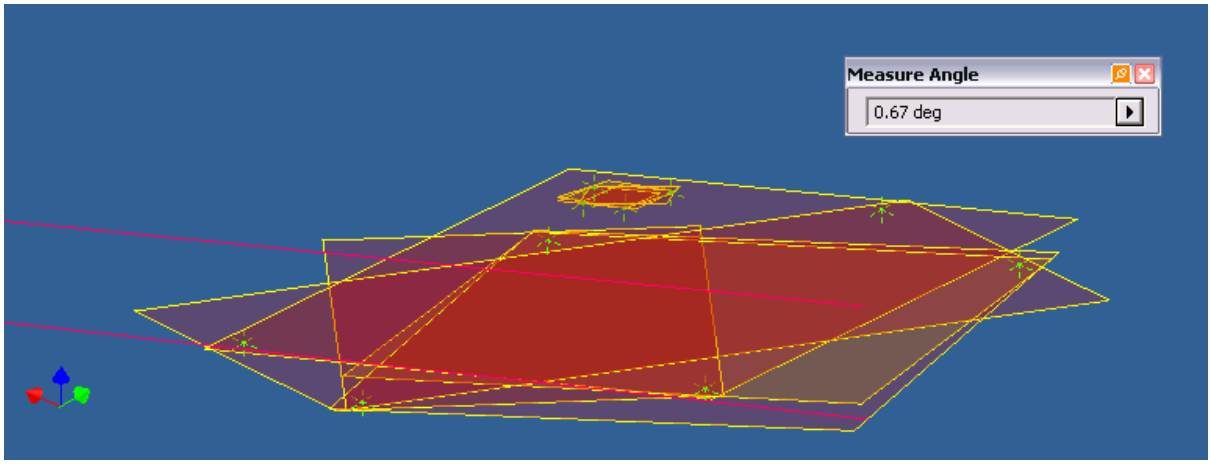

Figure 18: The results from the CMM measurements, with the xyz- coordinates (green stars) plotted in Autodesk® Inventor™. Work planes have been added to these coordinates, with the large planes representing the back plate, and the small planes representing the detector front. The angle measured between these two planes is shown.

The observed oscillations in the band pass are most likely to be due to channelling. This is due to multiple reflections or fabry-perot fringing between the filter layers or within the detector element itself, and appears to increase at longer wavelengths, made more prominent by the reduced signal in the far infrared. In the B3 channel, this channelling, combined with noise, dominates the spectra taken, making any spectral leaks impossible to be identified. Further experiments are needed to be conducted to see if this could be reduced, by either improving the detector electronics to increase the signal to noise ratio, or by improving the mounting jig, however the lack of any significant broadening has not yet been observed.

The spectral leak seen in the B1 filter will not change the spectral response of the channel in the actual instrument though, because the B1 channel has a blocker with a long-wavelength cut-off at 50 microns.

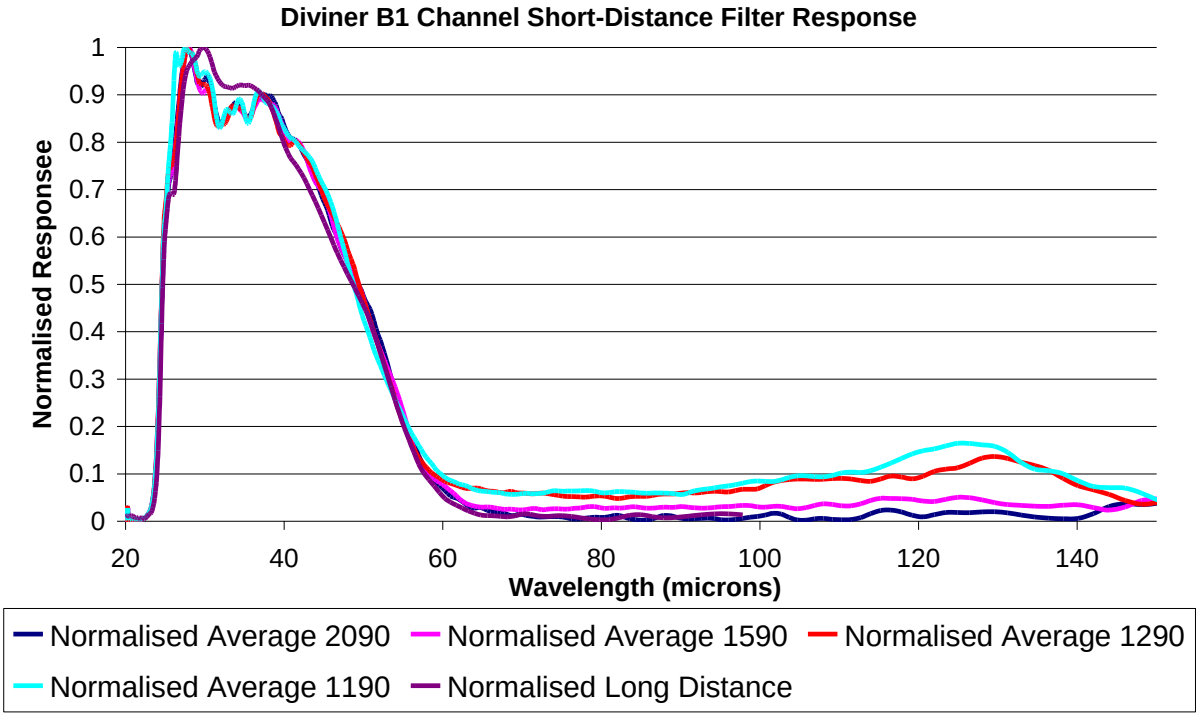

Figure 19: The spectral response of the B1 channel at various filter-to-detector distances. No systematic broadening of the channel is seen as the distance is reduced, but a plateau region is observed at beyond the long-wavelength cut-off. This plateau can clearly be seen to increase as the filter-detector distance is reduced, indicating that this is likely to be a spectral leak.

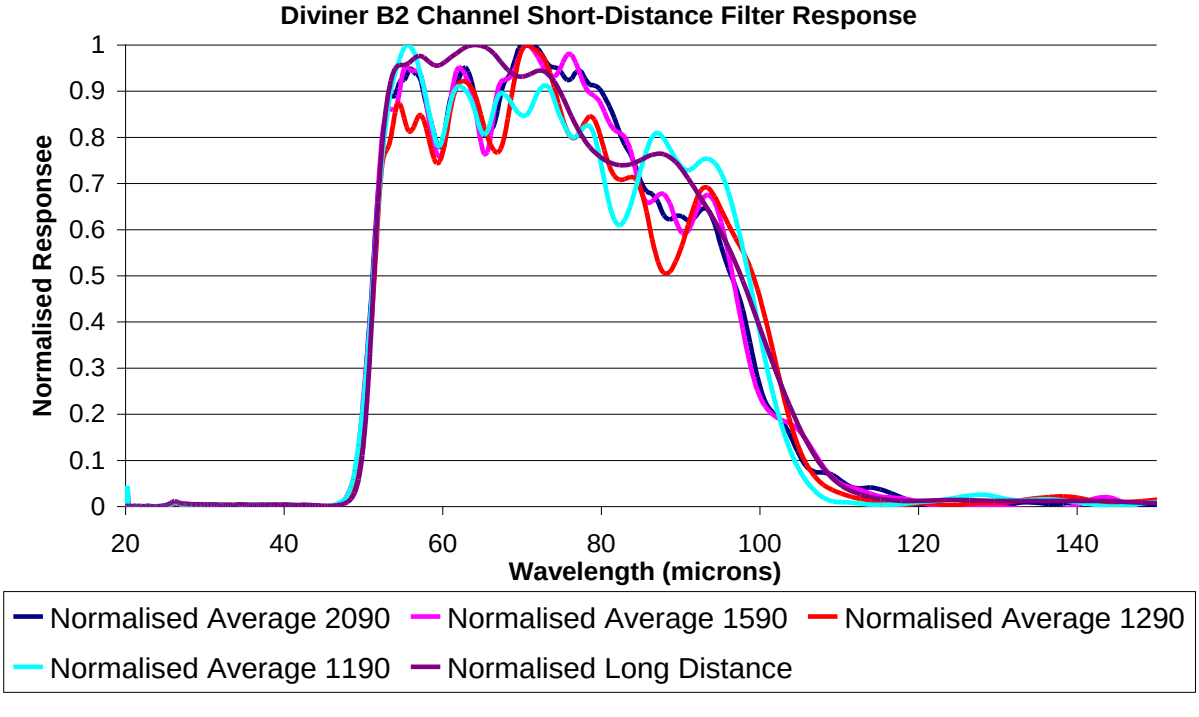

Figure 20: The B2 channel measured at various filter-to-detector distances. While there are considerable differences between the measurements of the long-wavelength cut-off, no trend is seen from smallest to greatest filter-detector distance. The differences could be due to "channelling" as can be seen throughout the entire spectra, or due to the low spectral resolution at high wavelengths.

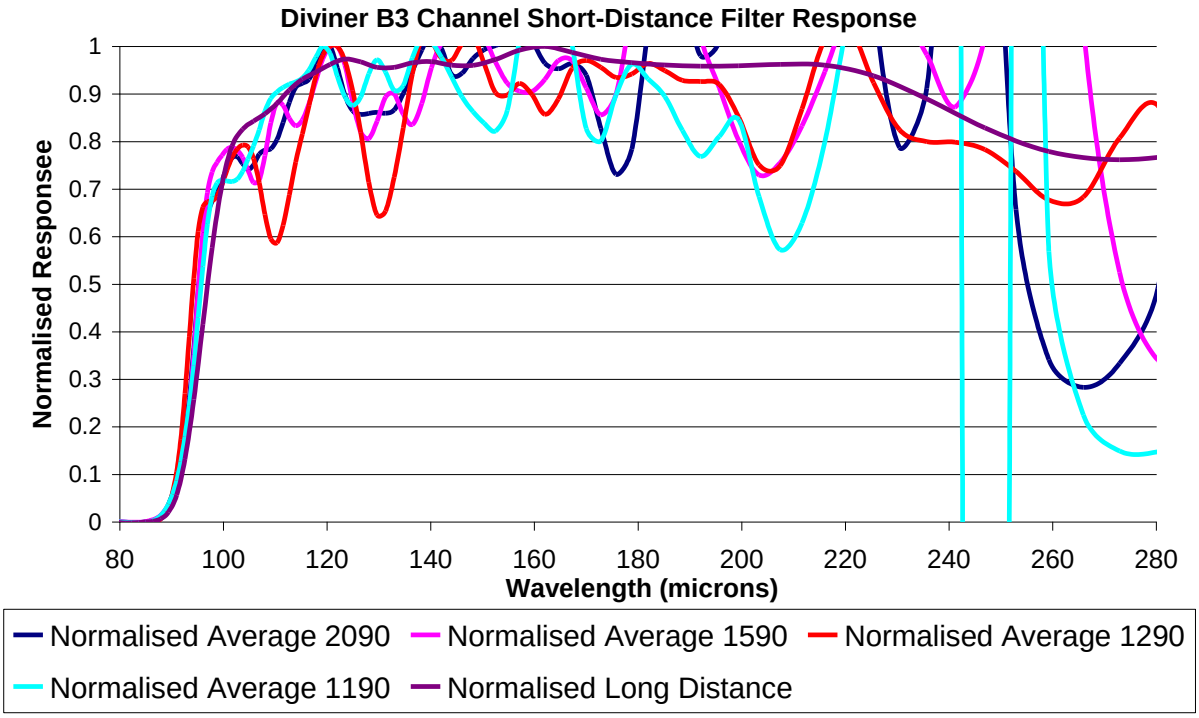

Figure 21: The B3 filter response at various filter-detector distances. The oscillations observed here, most likely due to channelling, are significant, therefore only the short-wavelength switch-on is shown. The lower signal in the far infrared means that the effects of channelling appear to increase with increasing wavelength, to the extent that the long-wavelength cut-off is indiscernible from these measurements

6 Laboratory Mineral Measurements

In order to constrain lunar surface composition using Diviner data, a spectral library of many different powdered lunar rock analogues is required. Because the Diviner channels cover such a wide range of wavelengths, and the lunar environment alters emission results [Murcray, 1970; Logan and Hunt, 1970; Henderson et al, 1996; Henderson and Jakosky, 1997 etc], currently available measurements will not suffice. Therefore, a new spectral library is required. While emission spectra taken in a simulated lunar environment are directly comparable to data returned from Diviner, the measurements take much longer (currently only one measurement is possible per day) and are more difficult and less accurate to calibrate effectively. Therefore, for initial measurements it is easier to use reflectance measurements and use Kirchhoff's Law (emission = 1 – reflectance) to convert from reflectance to isothermal (i.e. non-lunar environment) emission spectra. In future, these measurements allow comparisons to be made to previously published mineral spectra, and could be used to confirm mineral thermal gradient models. The lunar thermal environment enhances the contrast of the Christiansen Feature, without necessarily changing its peak wavelength, therefore matching this wavelength to returning data allows initial compositional constraints to be placed on the surface, until the lunar thermal environment emission results have been performed.

The samples chosen were all lunar regolith analogues, with specific emphasis on minerals that are expected to be the most distinct in terms of observations using the A3-A5 DLRE mineralogy channels.

6.1.1 Sample Selection

The list of minerals measured are shown in Table 2. Different particle sizes and many mixtures were also investigated in order to confirm how the Christiansen Feature varies with particle size distribution and mineralogical composition. The samples were obtained and prepared by Ben Greenhagen, a geologist from the University of California, Los Angeles (UCLA). Raman spectroscopy was conducted by John Hunt at UCLA, to verify the purity of the samples.

6.2 Diffuse Reflectance

The diffuse reflectance measurements were performed, jointly with Ben Greenhagen, using a Specac® Diffuse Selector Accessory specifically designed for use in the Brüker IFS 66v (Figure 22). A custom-built vacuum chamber was designed by Jon Temple and constructed by Jason Perry and Duncan Constable in the workshop at AOPP (Figure 23). It was constructed to fit inside the spectrometer sample chamber and be capable of containing the diffuse reflectance accessory, which was a complex task due to space limitations within the spectrometer. It was then attached to a turbo and roughing pump through the lid of the sample compartment (Figure 24).

Mineral/mixture	Grain size distribution (µm)	NIR	MIR	FIR
Anorthite	0-30	D	D, S	D
	30-64		D, S	
	64-120	D	D, S	D
	120-450		D	
Augite	0-30	D	D, S	D
	30-64		D, S	
	64-120	D	D, S	D
	120-450		D	
Enstatite	0-30	D	D, S	D
	30-64		D, S	
	64-120	D	D, S	D
	120-450		D	
Fayalite	0-30	D	D, S	D
	30-64		D, S	
	64-120	D	D, S	D
	120-450		D	
Forsterite	0-30	D	D, S	D
	30-64		D, S	
	64-120	D	D, S	D
	120-450		D	
Ilmenite	0-30		D, S	
	30-64		D, S	
	64-120	D	D, S	
	120-450		D	
Quartz	0-30		D, S	
	30-64		D, S	
	64-120		D, S	D
	120-450		D	
Albite	0-64		D	
	64-120		D	
	120-450		D	
Andesine	0-64		D	
	64-120		D	
	120-450		D	
Bytownite	0-64		D	
	64-120		D	
	120-450		D	
Diopside	0-64		D	
	64-120		D	
	120-450		D	
Labradorite	0-64		D	
	64-120		D	
	120-450		D	
Oligoclase	0-64		D	
	64-120		D	
	120-450		D	
FO25FA75 (25% Forsterite, 75% Fayalite)	0-30		D	
	30-64		D	
	64-120		D	

FO50FA50 (50% Forsterite, 50% Fayalite)	0-30		D	
	30-64		D	
	64-120		D	
FO75FA25 (75% Forsterite, 25% Fayalite)	0-30		D	
	30-64		D	
	64-120		D	
Mix 1	0-30		D	
	30-64		D	
	64-120		D	
Mix 2	0-30		D	
	30-64		D	
	64-120		D	
Mix 3	0-30		D	
	30-64		D	
	64-120		D	
Mix 4	0-30		D	
	64-120		D	
Mix 5	0-30		D	
	64-120		D	
Mix 6	0-30		D	
	64-120		D	
Mix 7	0-30		D	
	30-64		D	
	64-120		D	

Table 2: The minerals and mixtures, grain-size distributions and wavelength ranges that were successfully measured, where S = specular reflectance, D = diffuse reflectance, and E = emission. Some measurements could not be performed due to lack of signal (especially in the FIR or with 'dark' samples), and some were not needed. For example, the mixtures only needed to be measured in the mid-infrared to investigate changes in Christiansen Feature location, and many of the specular measurements produced the same spectral shape as the diffuse measurements (and took much longer to measure). Diffuse and emission measurements in the mid-infrared are the most important, because the compositional investigation is mainly interested in matching the CF peak found in laboratory measurements to returning lunar data. The setup and minerals are still available, so if more data does need to be taken, this can be done easily.

This allowed measurements to be conducted under: a) an overpressure of Nitrogen, b) a moderate spectrometer vacuum of approximately 10 mbar of dry, hydrocarbon filtered air, and c) a high vacuum of less than 10^{-3} mbar. To avoid breaking vacuum and to achieve accurate, in-situ calibration of these results, three samples and a reference standard were placed on a rotating stage at a time. This allowed the standard to be measured before and after each sample without breaking vacuum. The rotating stage, shown in Figure 25, consisted of a base, stepper motor and carousel containing sample cup holders, which held the sample being measured in the correct location and orientation. The stepper motor was under computer control.

Figure 22: The Specac® Diffuse Selector Accessory, inside the Brüker IFS 66v sample compartment. The white arrow indicates the location of the sample under investigation.

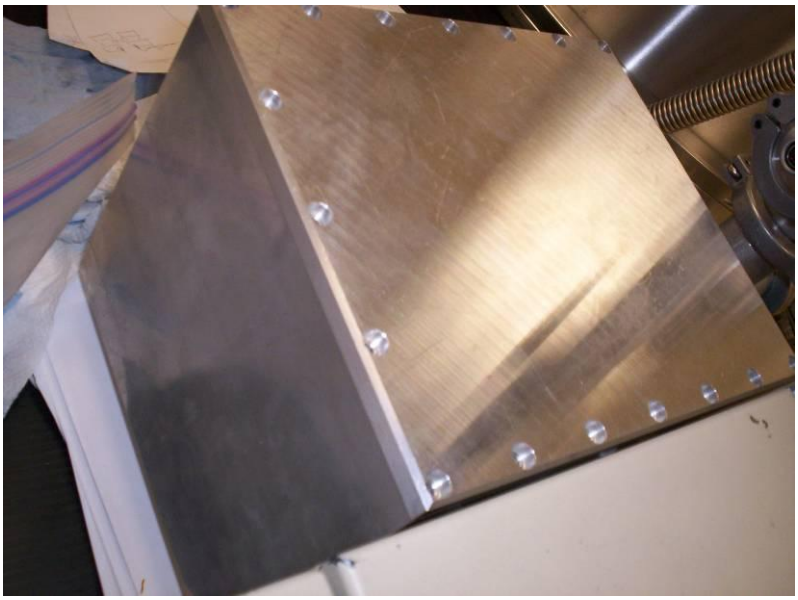

Figure 23: The vacuum chamber, designed by Jon Temple and constructed by Jason Perry and Duncan Constable in the AOPP workshop.

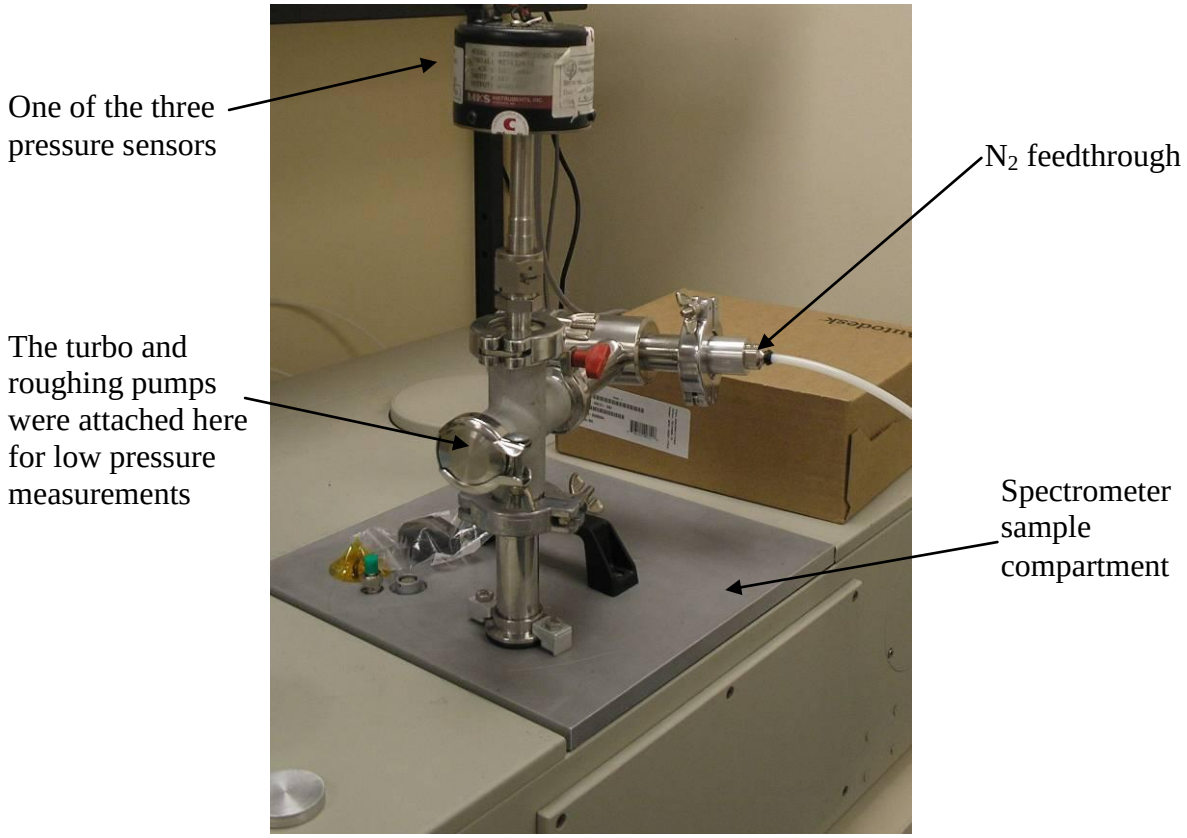

Figure 24: The Brüker IFS 66v with the vacuum chamber inside the spectrometer and vacuum piping coming through the sample chamber lid

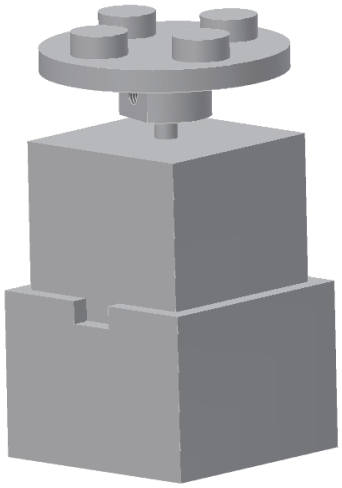

Figure 25: An Autodesk® Inventor™ CAD drawing of the stepper motor jig.

Several diffuse reflectance reference standards were used, chosen depending on which standard exhibited a measurable, spectrally-flat response in the region under investigation. For near- and mid- infrared readings, an aluminium target was used as the standard, which was determined to be spectrally flat by comparing it to a blackbody of known emissivity. The blackbody itself was not used, as it has a high emissivity and therefore very little reflectivity, and so could not be measured quickly between each sample.

The diffuse Al reference standard was made by machining a small cylinder of equal height as the sample cups, the top of which was then grit blasted to give a diffuse finish. The standard was then rotated and measured many times to ensure uniform, isotropic diffusivity. This reference showed insufficient signal to be measurable in the FIR wavelength region though, and so a sample cup filled with crushed polypropylene was instead used for these measurements. Large polypropylene granules were frozen in liquid nitrogen and ground into small particulates, which were then placed in a sample cup and used for this purpose.

Before measuring in the spectrometer, samples were placed in sample cups and the top surfaces smoothed with a glass slide to achieve true reflectance measurements, as in Figure 26. The samples were then placed in a vacuum oven at 50°C for at least 2 hours in order to remove contaminants such as water vapour, which may have been absorbed from the air prior to heating. The samples being investigated were then moved immediately from the vacuum oven into the spectrometer which was immediately evacuated of air. To increase the speed and efficiency of taking measurements, ~15 more sample cups were made.

Spectra were acquired in the near- infrared using a 5mm aperture, 4x gain, with a scanner velocity of 10kHz, at a resolution of $4cm^{-1}$, with 512 scans averaged per measurement. Each MIR spectra consisted of 800 scans, taken using a 10mm aperture, 4x gain, 7.5kHz scanner velocity with a $4cm^{-1}$ resolution. Much lower signals were observed in the FIR region, and so a 12mm aperture was used, at 1.6kHz with 16x gain. These scans were slow due to the low scanner velocity, so 400 scans were performed with a resolution of only $8cm^{-1}$. Even after making these adjustments to the spectrometer setup, the signal to noise ratio of most of the interferograms were too low to be measured, and so most FIR reflectance measurements were omitted (Table 1). Emission of these samples will be measured instead in future, which should provide better results, as the samples should have emissivities > 0.8. Combinations of beamsplitters, detectors and sources were used, as described in section 11.6, to measure spectra at wavenumbers between the NIR, MIR and FIR ranges. Some selected results from the diffuse reflectance measurements are shown in Figure 27, Figure 28 and Figure 29.

To verify the results, the 0-32 micron grain size samples are currently being measured by the RELAB facility at Brown University, Rhode Island, USA, and by Tim Glotch at Stony Brook University, New York, USA.

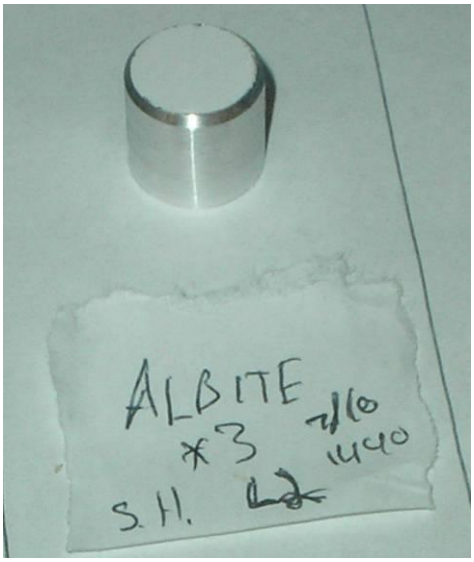

Figure 26: A photo of a new-design sample cup, containing Albite, placed in the vacuum oven at 50°C to remove water vapour from the powdered rock. The *3 indicates that this sample is composed of 0-64µm size particles, along with the sample cup number and date and time in which it was placed in the vacuum oven. The samples were smoothed to ensure a uniform, level surface for accurate reflectance measurements to be performed.

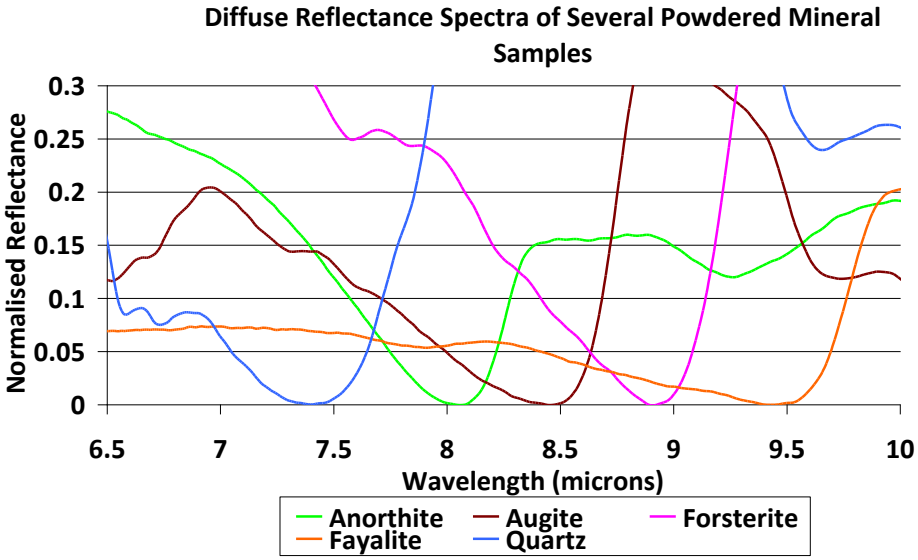

Figure 27: The graphs shows diffuse reflectance spectra for some of the minerals measured, with particle sizes of 64-120µm, magnified to highlight the differences in Christiansen Feature location. The spectra were found by dividing by the diffuse Al reference and normalising to have a maximum of 1 and a minimum of 0. In general, the CF shifts to longer wavelengths with increasing abundance of mafic minerals, from Quartz to Fayalite, as expected [Salisbury et al, 1997].

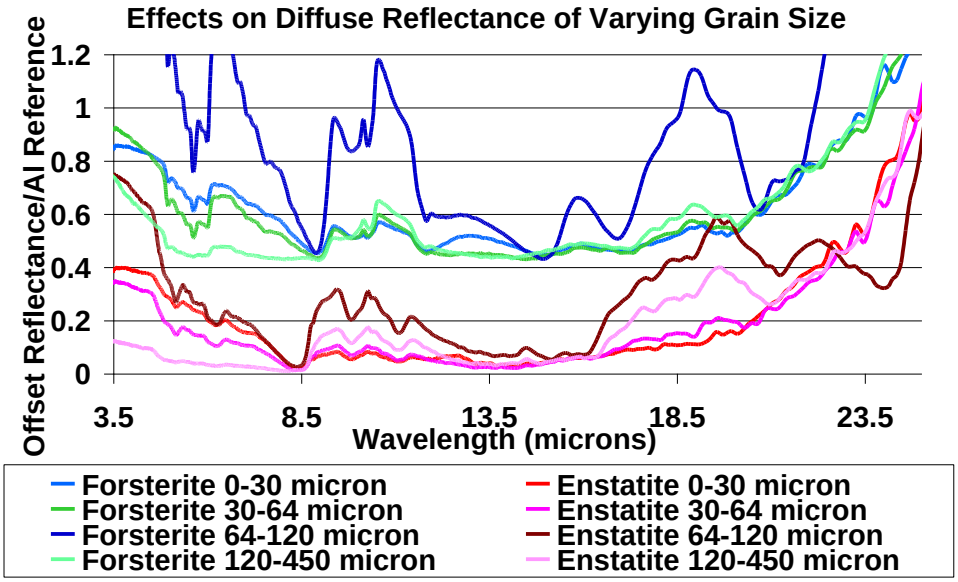

Figure 28: The effect of varying grain size on diffuse reflectance measurements. The band contrast is seen to reduce for increased grain sizes at the CF reflectance minima around 8.5 microns, except for the 64-120 micron grain size sample.

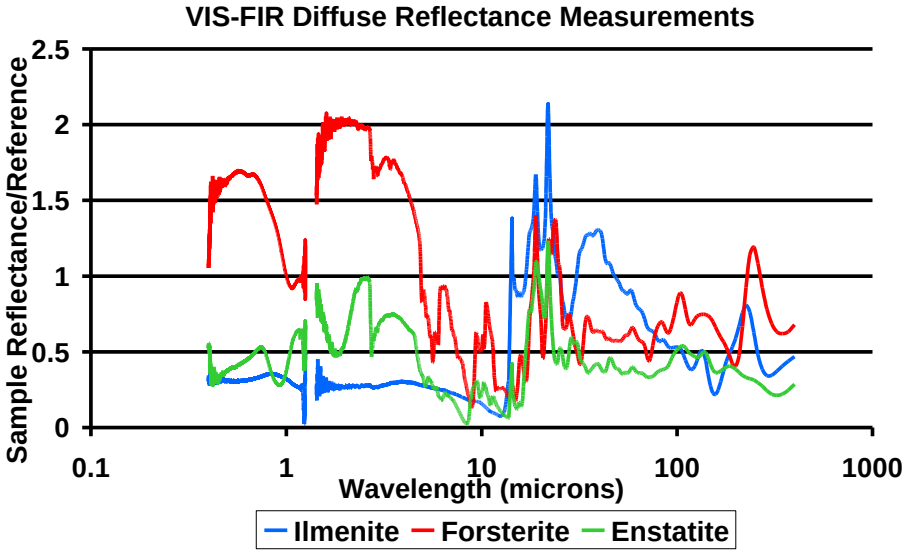

Figure 29: Combined VIS/NIR, MIR and FIR spectra across almost all of the wavelength ranges measurable by Diviner. In some regions of the spectrum, the minerals are more diffusely reflecting than the diffuse reflectance standard used, hence reflectances higher than 1 are observed.

6.3 Specular Reflectance Measurements

A Perkin Elmer® Specular Reflectance Kit was modified to allow mineral samples to be measured whilst in the sample cups (Figure 30). Originally, the kit could only be used to measure solid surfaces, as the samples were required to be suspended upside down, so new apparatus was built to allow the kit to stand inverted, with samples sat below. Due to the lack of space in the chamber below the kit, a motorised sample changer could not be used, so vacuum had to be broken between each measurement. The reference standard used was again the diffuse aluminium disc, which was measured against a gold mirror, the reference standard supplied with the specular reflectance kit. The gold mirror was not used as the standard, because most of the minerals were poor specular reflectors, and so the spectrometer settings used to measure the samples then saturated the detector when the gold was used. The diffuse Al disc had a specular reflectance more similar to the minerals, and so everything could be measured using the same gain, aperture and scanner velocity settings. Some results are shown in Figure 31.

6.4 Emission Measurements – The Lunar Environment Simulator

6.4.1 Initial Design

Due to the lunar environment, samples exhibit different spectral shapes than the same samples measured on a planet with an atmosphere [Henderson and Jakosky, 1997; Hapke, 1996]. This effect is manifested as an emission maximum with a peak at around 8 microns in the mid infrared (section 2.4.1). In order to accurately analyse the Diviner data to constrain surface composition, this effect must be recreated and measured in the laboratory. The vacuum chamber used for very low pressure diffuse reflectance measurements was modified for this purpose.

As space is limited inside the chamber, the samples could not be heated by incident solar-like radiation, as is the case on the Moon, but instead from below. This produces the same effect as direct solar heating, as the diurnal wave penetrates several tens of centimetres into the lunar surface, and also prohibits any reflected component from being included in the emission spectra. Heating from below has been shown to produce equal results to heating from above [Henderson and Jakosky, 1994 and 1997; Henderson et al, 1996], as an equal thermal gradient can be achieved as occurs on the lunar surface. Inside the chamber, this heating was achieved by placing one sample at a time on a circular disc, which had Lakeshore® Nichrome resistance heater wire wrapped around it.

To produce a thermal gradient in the sample, a box painted with Nextel™ Black paint was placed above the sample, which was cooled using liquid Nitrogen. The first design used a Copper cold finger to provide this cooling power, which was hard soldered through the centre of a 49.5mm steel disc. Stainless steel is a poor thermal conductor, and the disc was machined as thin as was possible (to ~2mm), therefore preventing the cooling power from being dissipated through the chamber walls. This disc was then secured into one of the window ports in the chamber, with the black-painted box and an off-axis paraboloid (OAP) attached onto the cold finger. An extra Aluminium cylinder was made to attach to both the box and the cold finger, with a large surface area in contact with both parts, aiding in transferring the cooling power to the box. The OAP reflected radiation emitted from the sample, through the other window port in the chamber, and into the spectrometer emission port, with the correct beam width and shape to enter the Brüker IFS 66v spectrometer.

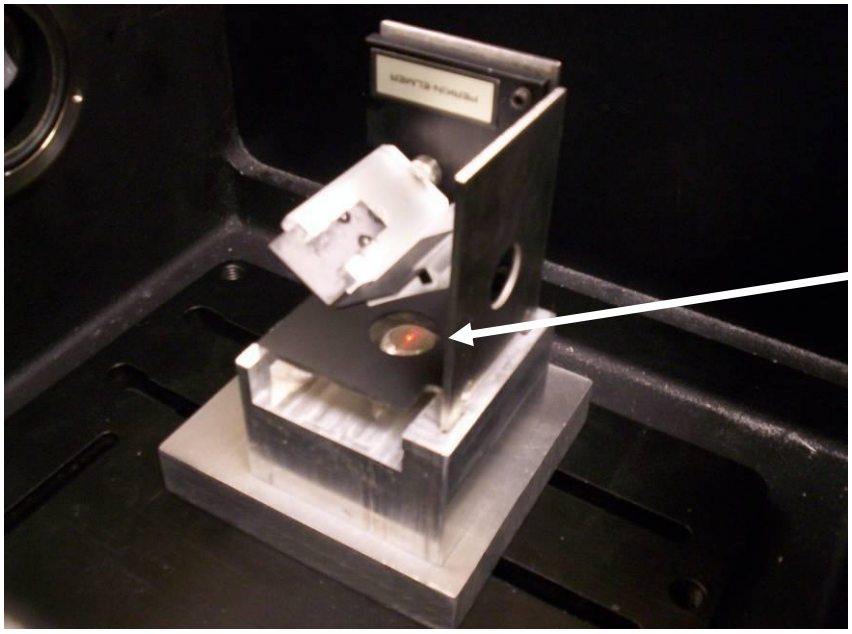

Figure 30: The Perkin Elmer® Specular Reflectance Kit, placed on the custom-built apparatus, allowing it to be used upside down. The sample being measured is indicated by the white arrow.

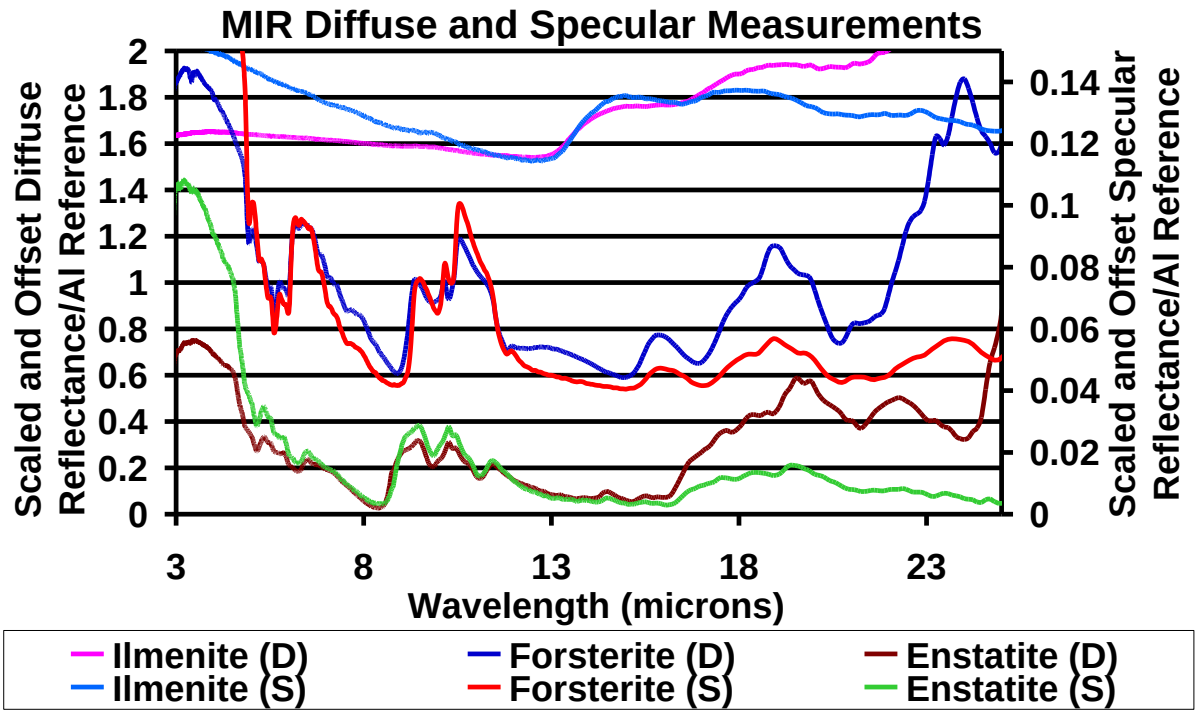

Figure 31: A plot showing both diffuse and specular reflectance results. The lines have been scaled and offset in the y-direction to make the different mineral spectra distinguishable. The diffuse and specular reflectance spectra are observed to exhibit identical spectral features, though the specular features are less pronounced.

The emission port of the spectrometer accepts a diverging beam of focal length 153mm, with a focal point approximately 20mm from the outside wall of the spectrometer, as shown in Figure 40. Due to the width of the chamber wall and location of the OAP within the chamber, this beam has already passed the focal point and therefore the spectrometer input beam is converging by the point at which it is incident on the paraboloid. The sample emits a diverging beam, and therefore ideally an elliptical mirror would be needed to direct the sample emission into the Brüker spectrometer. Bespoke elliptical mirrors are very expensive, and hence an appropriate OAP was used instead. A simple ray tracing diagram, shown in Figure 32, shows that this was a suitable mirror to use instead.

A vacuum-compatible KBr window was placed in the port through which the emitted radiation passed into the spectrometer, and a turbo pump was attached to the chamber, capable of pumping down the box to below 10^{-3} mbar, to replicate the very low pressure of the Moon. All the electrical connections (i.e. sensors, heater wire and later the stepper motor) were fed through a vacuum-compatible 15-pin Fischer® connector.

6.4.2 Improvements

Unfortunately, this first design was not as successful as expected, as the cooling power of the cold finger was only sufficient to cool the box to a minimum of -50°C. Much lower temperatures than this are needed to set up the sharp thermal gradients in the sample, as experienced on the surface of the Moon [Henderson and Jakosky, 1997]. Also, it was discovered that the K-type thermocouples gave different readings to the PRT and RTD temperature sensors. This was because thermocouple feed-throughs were not used to pass the signals out of the chamber, and so each extra thermocouple junction introduced a temperature error.

The thermocouples were replaced with adhesive RTD temperature sensors, and a liquid nitrogen feed-through was made to cool the box and OAP to much lower than -50°C. This consisted of two Copper pipes hard-soldered through a stainless steel flange, connected using Swagelok™ fittings to more copper piping, which were soft soldered to a Copper plate attached to the box. A diagram of the apparatus is shown in Figure 33.

This setup produced some unexpected results. The spectra of a blackbody placed in the location of the sample changed when the temperature of the box was varied. One of the tests that was performed was to measure the emission of a blackbody (high emissivity), diffuse aluminium disc (medium emissivity), and gold mirror (low emissivity) all held at 60°C, while the box was lowered. At certain box temperatures, the relative emissivity of the three targets varied, indicating something was not working as expected. After mapping the field of view of the spectrometer emission port, it was found that emission from the cooled box was also be measured by the spectrometer. On further consultation with Brüker, it was found that the incidence cone expected by the emission port did not converge to a point source as expected, and had a finite size at its focus. This meant that the actual field of view of the spectrometer was actually like Figure 34 rather than Figure 32.

This affected the results significantly, due to way that a fourier transform spectrometer works: A signal with the same radiance as the ambient spectrometer interferes destructively with the spectrometer, causing no interferogram to be seen and hence no spectra to be recorded. Likewise, a sample at a temperature below ambient will produce a negative signal, as seen in Figure 35.

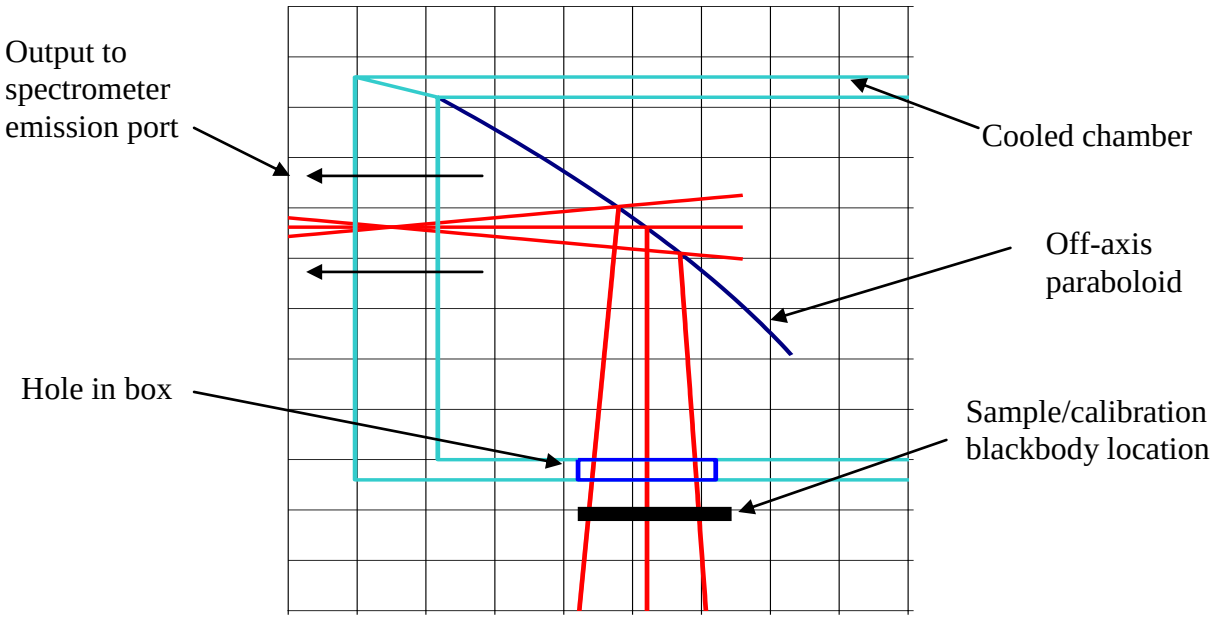

Figure 32: A simple ray-tracing diagram showing how the beam from the sample was expected to be reflected into the spectrometer emission port at the correct angle.

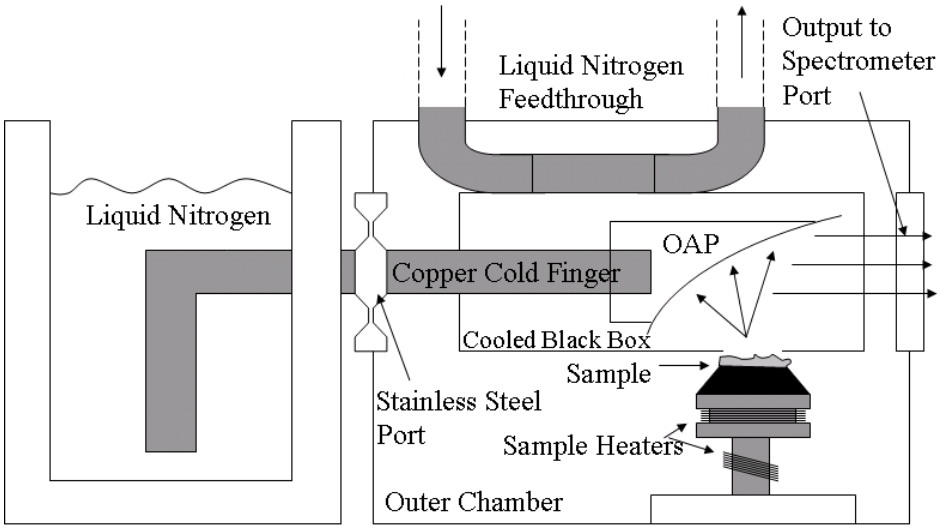

Figure 33: The emission apparatus after addition of the liquid nitrogen feed-through.

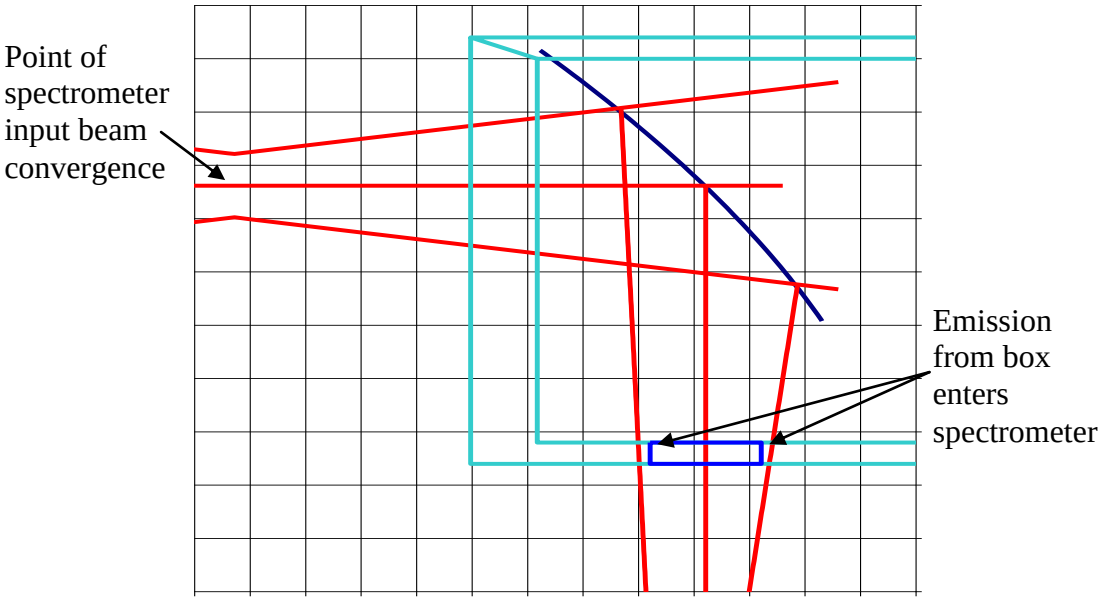

Figure 34: A simple ray-tracing diagram showing how the beam is changed by the finite width at the point of convergence and the part of the box around the hole that is included in the emission measurement.

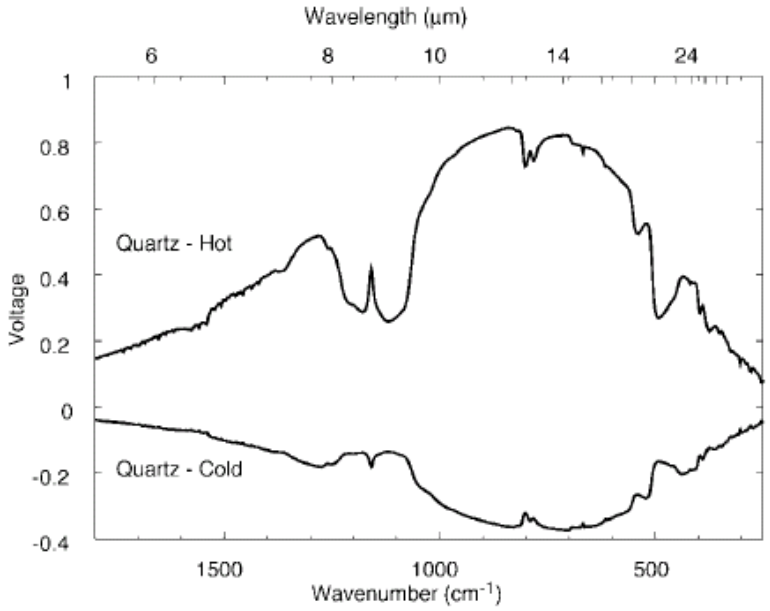

Figure 35: Emission of heated and cooled quartz particulates measured by Baldridge and Christensen 2009.

A baffle was made and placed inside the spectrometer to remove the emission measured from the cooled box, but this was found to reduce the wanted signal. There were other concerns about this setup: The sample was located too close to the OAP and output beam port, meaning that radiation from spectrometer had a direct line-of-site to the sample, so the field of view of the sample was not completely filled with cooled box. Also, the close proximity of the sample to the underneath of the box meant that the cooling power of the box may be stronger than under true lunar conditions. Finally, the Swagelok® fittings used in the liquid nitrogen feed-through occasionally failed and had to be replaced several times. Taking all these problems into account, a new lunar environment simulator was designed and built.

6.4.3 The Final Lunar Environment Simulator

The final setup is shown in Figure 36. The cold finger has been completely removed and the liquid nitrogen feed-through has been run through the port instead, negating the need for Swagelok® connectors. A stepper motor and pulley system has also been included to allow the sample being measured to be changed without breaking vacuum. Up to two samples and a black painted disc, for calibration purposes, can be placed on the carousel at any one point. A joint window assembly has also been made for the output window on the box and the emission input port on the spectrometer, meaning only one KBr window has to be used to keep both the chamber and the spectrometer under their vacuums. This assembly also permanently attaches the chamber to the spectrometer, preventing changes between experiments.

Some simulated lunar environment emission results from this setup are shown in Figure 37. As can be seen, there are still some calibration issues due to the difficulties in converting raw spectra to calibrated radiances, which are causing the baseline to appear to tilt. The noise seen in the spectra is due to the processing required to calibrate radiances, which is derived from measurements of a blackbody, which will be improved as more blackbody spectra are taken.

Once sufficient emission spectra have been taken and correctly calibrated, these will be convolved to the spectral responses of the Diviner channels. The relative magnitudes of the mineral spectra for each channel can then be compared to the data returned from the instrument.

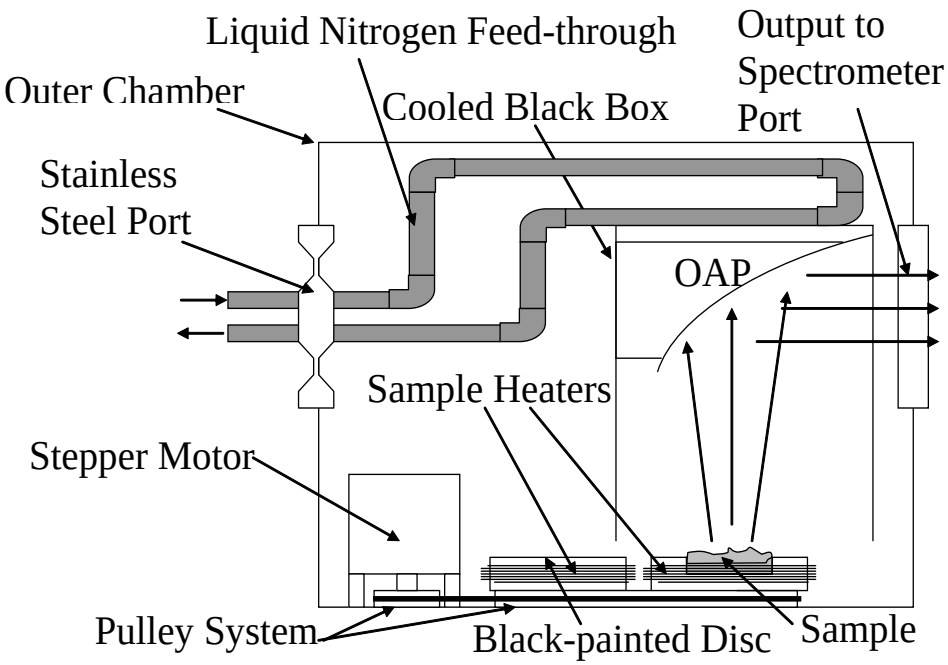

Figure 36: The final design for the Lunar Environment Simulator.

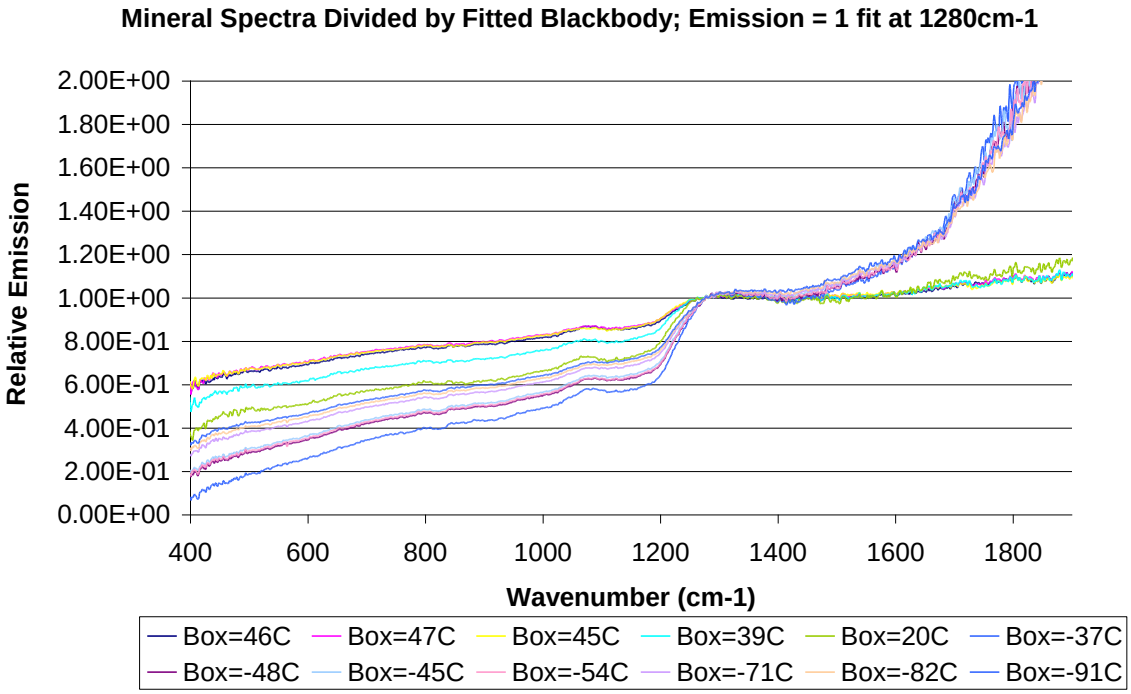

Figure 37: Mid infrared spectra of Anorthite composed of 0-32 micron sized grains. The graphs have been normalised so that the Christiansen Feature emissivity peak, at approximately 1280cm^{-1}, is displayed with an emissivity of 1. The graph shows that as the box is cooled, the peak is enhanced, as expected. The calibration of the emission spectra still needs more work, as the baseline either side of the CF should be relatively flat, not sloping as is observed. The calibration was performed in the usual method for calibrating fourier transform spectrometers, by recording the emission spectra of a black disc at various temperatures [Maturilli et al, 2006; Baldridge and Christiansen, 2009 etc]

7 Data Analysis

Diviner has now returned more than a month of data, which although the satellite is still in its elliptical commissioning orbit, can be used to begin the initial analysis.

The B3 channel data, which is capable of mapping the lowest temperatures of all the channels, was split into two equal datasets, to show the difference in temperatures as the local time of day changes. These are shown in

<Image of unpublished data removed for online publication>

Figure 38.

An initial composition map was made by plotting the wavelength of the Christian Feature emission peak, as shown in Figure 39. Three Diviner channels are located around this emissivity maximum, and so a simple quadratic was fit through the brightness temperature returned from each channel. Brightness temperature is derived from fitting a Planck Function to the radiance, assuming an emissivity of 1. The wavelength of the peak was then derived from calculating the maximum value of this curve, by finding where the derivative of the curve is equal to 0. This is currently the 'standard' algorithm [Greenhagen, private communication 2009].

When the spacecraft begins to take data near lunar midday, which will occur in September, this type of compositional map will improve. With the Sun directly overhead, the greatest thermal gradients occurring on the Moon will be present, causing maximum enhancement of the Christiansen Feature.

<Image of unpublished data removed for online publication>

Figure 38: Some initial Diviner B3 brightness temperature data from 6th July to 12th August, split into two equal datasets, showing the south pole region below -80° latitude. The variations in temperatures due to the change in local hour are visible.

<Image of unpublished data removed for online publication>

Figure 39: A Mercator map of the Moon, showing the wavelength of the Christiansen Feature calculated by plotting a quadratic through Diviner channels A3-A5 [Paige, personal communication 2009]. The data already shows clear distinctions between the highlands (yellow, red and pink) and the mare (blue). More data taken closer to midday will improve this map significantly, especially on the far side of the Moon (left of the diagram), where the data used to derive this map was taken at a late afternoon local hour.

8 Future Work

8.1 Continue with Emission Measurements

Now that a working lunar environment simulator has been constructed, and has demonstrated the ability to enhance the Christiansen Feature when minerals are measured in a lunar thermal environment, the procedure for converting raw spectra to emissivity needs to be further refined. As can be seen in Figure 37, more work needs to be performed to fully calibrate the system for mineral emissivities to be derived accurately. Analysis of spectra already taken suggests that a blackbody, instead of a black disc, may need to be made for this purpose, but more investigation is still required.

Once the spectrometer has been calibrated, emission spectra of more samples can to be taken. These spectra will then be added to an online spectral library, for use by other Diviner team members. The website has been created and already contains the reflectance data, but is currently offline until the emission measurements have been performed.

8.2 Diviner Radiometric Calibration Validation

The analysis of radiometric calibration data was performed last year [Thomas, 1st year report, 2008], which determined the linearity of the channels. In space, the instrument is calibrated by occasionally viewing cold space and viewing a hot internal blackbody, between viewing the lunar surface. The number of counts measured from viewing the surface is converted to a radiance by interpolating between the two calibration views. Calibration on the ground was performed in a vacuum chamber at the Jet Propulsion Laboratory in Pasadena, California, USA, using a cooled blackbody to represent cold space, and a variable temperature blackbody to represent the surface. By recording the number of counts measured when viewing all three blackbody targets, the expected radiance of the variable temperature target was calculated from interpolating between the two calibration targets. This was plotted against the actual radiance of the variable target, producing a linearity curve for every pixel of every detector.

Diviner is currently in mapping mode in orbit around the Moon and using a simple linear interpolation between the two calibration sources (i.e. cold space and the internal blackbody target), instead of using the coefficients calculated from the radiometric calibration. The plots produced are sufficiently linear that the instrument can meet its requirements (section 11.5) using a linear interpolation routine, and that the many uncertainties within the calibration procedure could be the cause of the slight non-linearity observed. These uncertainties include: reflections due to the non-unity emissivity of the blackbodies, differences due to focal plan assembly temperature changes, fluctuations and accuracy of determining blackbody temperatures, errors in the spectral responses of the filters, and uncertainties in the removal of thermal lag from the data [Schofield, personal communication 2009]; some of which are extremely difficult to properly quantify.

In the future, a non-linear interpolation algorithm may be made for the channels to reduce the uncertainty in measured radiances, especially for the B3 and possibly also for the B2 channel, as these exhibited the most non-linear behaviour.

8.3 Using Diviner Data and New Mineral Spectra to Model Properties of an Area of the Lunar Surface

If sufficient data is returned from mid-latitude regions at lunar midday, then compositional analysis can begin. In the simplest initial studies, the wavelength of maximum emission and shape of the Christiansen Feature from channels A3-5 will be compared to mid infrared mineral emission data taken in simulated lunar conditions.

Once sufficient mineral spectra have been measured in the far infrared region, this data will be compared to the longer wavelength A6-B3 channels. Fits to the A1-2 channels or to Clementine NIR data could also be made by comparing the data to mineral reflectance measurements made in the visible/near infrared.

The effects of topography will initially be neglected, with the compositional study concentrating on relatively flat regions (i.e. not steep crater walls). Once sufficient data has been returned from the LOLA instrument, or when the LALT instrument team onboard SELENE makes its data publicly available, then topographic effects can be studied.

Research needs to be conducted into new techniques for analysing the returning data. Currently, fitting the mineral spectra to the Diviner data simply involves calculating the relative radiances expected to be observed by the Diviner channels for each mineral, and comparing these directly to the Diviner data. If a more mathematical method, such as Singular Value Decomposition (SVD) or Principal Component Analysis (PCA) could be used to extract more compositional information from the available data, this would be advantageous.

Rock abundances measurements need data for areas of the surface measured across a full diurnal cycle before data can be fitted to a plot such as that seen in Figure 3, therefore such analysis has not been performed yet. The instrument will map a full diurnal cycle every six months, hence the first cycle will be completed in January.

Once new emission data has been measured in the mid- and far-infrared, this data could be used to reduce the uncertainty of the instrument in determining surface temperature. Calculated brightness temperatures currently assume that the emissivity of the surface is equal to 1. If a more realistic emissivity could be used, surface temperatures could be determined more accurately.

A Gantt Chart showing the expected completion dates of each major component of future work is shown in Table 3.

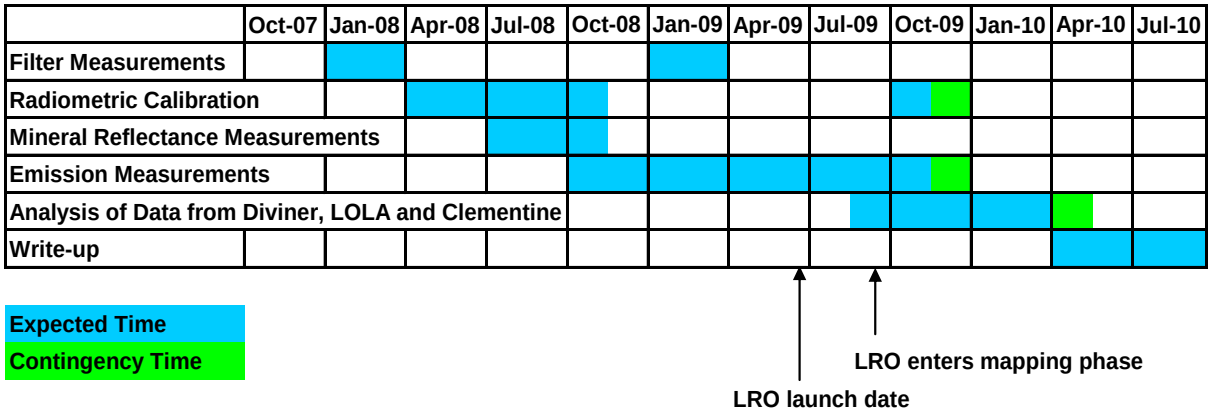

Table 3: A Gantt Chart showing approximate dates of completion for the various stages of the D.Phil Project. Expected times are shown in blue, while contingency times are shown in green.

9 Acknowledgements

I would like to thank everyone for their invaluable help over the past year, but along with my supervisors, special thanks must go to: Jon Temple, Andy Clack, Duncan Constable, Jason Perry, Bob Watkins, Ramin Lolachi, Adam Camilletti from AOPP; John Hunt from UCLA (now at JPL); and to Ben Greenhagen, David Paige, Tim Schofield, Marc Foote, and all the other members of the Diviner Science Team.

10 Bibliography

Arnold, J. R., 1979. Ice in the Lunar Polar Regions". J. Geophys. Res. Vol. 84, pp.5659-5668

Baldridge, A. M. and Christensen, P. R., 2009. "A Laboratory Technique for Thermal Emission Measurement of Hydrated Minerals". Applied Spectroscopy. Vol. 63, pp. 678-687

Benz, W., Slattery, W. L. and Cameron, A. G. W., 1986, "The origin of the moon and the single-impact hypothesis I". Icarus. Vol. 66 (3), pp. 515-535

Campbell, B. A. et al, 2003. "Radar Imaging of the Lunar Poles". Nature Vol. 426, pp. 137-138

Chin, G. et al, 2007. "Lunar Reconnaissance Orbiter Overview: The Instrument Suite and Mission". Space Sci. Rev. Vol. 129, pp.391–419

Cooper, B. L. et al, 2002. "Midinfrared Spectral Features of Rocks and Their Powders". J. Geophys. Res. Vol. 107, pp. 1-16

Farmer, V. C. (ed.), 1974. "The Infrared Spectra of Minerals". Mineralogical Society of Great Britain & Ireland. Surrey: Adlard & Son Ltd.

Feldman, W. C. et al, 1998. "Evidence for Water Ice near the Lunar Poles". Science Vol. 281, pp. 1496-1500

Foing, B. H. et al, 2006. "SMART-1 mission to the Moon: Status, first results and goals". Advances in Space Research Vol. 37 (1), pp. 6-13

Foote, M, T., 2008, "DLRE Radiometric Test Report JPL D-42958". unpublished draft

Gaidos, E. et al, 2006. "Terrestrial Exoplanet Light Curves". Proc. International Astronomical Union Colloquium No. 200, pp. 153-158

Glotch, T. D. et al, 2007. "Mid-infrared (5-100 μm) Reflectance Spectra and Optical Constants of Phyllosilicate Minerals". Icarus Vol. 192, pp. 605-622

Greenhagen, B. T. & Paige, D. A., 2006. "Mapping Lunar Surface Petrology Using the Mid-Infrared Emissivity Maximum with the LRO Diviner Radiometer". 37th Annual Lunar and Planetary Science Conference, no. 2406.

Greenhagen, B. T. & Paige, D. A., 2009. "Overview of the 2009 LRO Diviner Lunar Radiometer Compositional Investigation". Lunar and Planetary Institute Science Conference Abstracts Vol. 40, pp. 2255-2256

Hanel, R. A. et al, 2003. "Exploration of the Solar System by Infrared Remote Sensing". Cambridge: Cambridge University Press

Hapke, B., 1996. "A model of radiative and conductive energy transfer in planetary regoliths". J. Geophys. Res. Vol. 101, pp. 16817-16831

Haruyama, J. et al, 2008. "Lack of Exposed Ice Inside Lunar South Pole Shackleton Crater". Science Vol. 322, pp. 938-939

Heiken, G. H. et al, 1991. "Lunar Sourcebook – A User's Guide to the Moon". Cambridge University Press, 1991

Henderson, B. G. & Jakosky, B. M., 1994. "Near-surface thermal gradients and their effects on mid-infrared emission spectra of planetary surfaces". Journal of Geophysical Research Vol. 99, pp. 19063

Henderson, B. G., et al., 1996. "New laboratory measurements of mid-IR emission spectra of simulated planetary surfaces". Journal of Geophysical Research Vol. 101, pp. 14969-14975

Henderson, B. G. & Jakosky, B. M., 1997. "Near-surface thermal gradients and mid-IR emission spectra: A new model including scattering and application to real data". Journal of Geophysical Research Vol. 102, pp. 6567-6580

Jolliff, B. L. et al (eds.), 2006. “New Views of the Moon”. Mineralogical Society of America: Reviews in Mineralogy & Geochemistry Vol. 60

Kerr, R. A. (ed.), 2009. “A Primal Crust Found on the Moon, While Mercury’s Proves Elusive”. Science Magazine Vol. 324, pp. 161

Lawrence, D. J., 1998, “Global Elemental Maps of the Moon: The Lunar Prospector Gamma-Ray Spectrometer”. Science Vol. 281, pp1484-1489

Logan, L. & Hunt, G. R., 1970. "Emission spectra of particulate silicates under simulated lunar conditions". Journal of Geophysical Research Vol. 75, pp. 6539-6548

Logan, L M., et al., 1973. "Compositional Implications of Christiansen Frequency Maximums for Infrared Remote Sensing Applications". Journal of Geophysical Research Vol. 78, pp. 4983-5003

Maturilli, A., et al., 2006. "Emissivity measurements of analogue materials for the interpretation of data from PFS on Mars Express and MERTIS on Bepi-Colombo". Planetary and Space Science Vol. 54, pp. 1057-1064

McCleese, D. J. et al, 2007, “Mars Climate Sounder: An investigation of thermal and water vapour structure, dust and condensate distributions in the atmosphere, and energy balance of the polar regions”. J. Geophys. Res. Vol. 112, E05S06

Mendell, W. W. & Low, F. J., 1974. "Preliminary Results of the Apollo 17 Infrared Scanning Radiometer". Moon Vol. 9, pp. 97-103

Mendell, W. W. & Wieczorek, M. A., 1993. “Thermogeologic Mapping of the Moon from Lunar Orbit”. Lunar and Planetary Inst., 24th Lunar and Planetary Science Conference. Part 2: G-M pp. 977-978

Mignard, F., 1979. "The evolution of the lunar orbit revisited. I". Moon and Planets Vol. 20, pp. 301-315

Murcray, F. H., et al., 1970. "Infrared emissivity of lunar surface features. 1. Balloon-borne observations.". Journal of Geophysical Research Vol. 75, pp. 2662-2669

Nightingale, T. J., 1992. “Aspects of the Radiometric Performance of the Improved Stratospheric and Mesopheric Sounder”. Ph.D. Thesis

Nozette, S. et al, 1996. “The Clementine Bistatic Radar Experiment”. Science Vol. 274, pp. 1495-1498

Nozette, S., et al., 1994, “The Clementine mission to the Moon: Scientific overview”. Science Vol. 266 (5192), pp.1835-1839

Paige, D. A., et al., 2009. "The Lunar Reconnaissance Orbiter Diviner Lunar Radiometer Experiment". Space Science Reviews Vol. pp. 66

Paige, D. A., unknown year, “Diviner LRO Proposal AO NNH04ZSS003O; Measurement Investigation and Implementation”. Initial DLRE mission proposal.

Pieters, C. M., et al., 1993. "Optical effects of space weathering on lunar soils and the role of the finest fraction". Lunar and Planetary Institute Science Conference Abstracts Vol. 24, pp. 1143-1144

Presley, M. A. & Christensen, P. R., 1997. "Thermal Conductivity Measurements of Particulate Materials 2. Results". J. Geophys. Res. Vol. 102, pp. 6551-6566

Salisbury J. W. et al, 1997. "Thermal Infrared Spectra of Lunar Soils". Icarus Vol. 130 (1), pp. 125-139

Sanderson, K., 2007, "The sunniest spot on the Moon". Nature News [online] 23rd October

Spencer, J. R. et al, 1989. "Systematic Biases in Radiometric Diameter Determinations". Icarus Vol. 78, pp. 337-354

Spencer, J. R., 1990, "A Rough-Surface Thermophysical Model for Airless Planets". Icarus Vol. 83, pp. 27-38

Tompkins, S. & Pieters, C. M., 1999. "Mineralogy of the Lunar Crust: Results from Clementine". Meteoritics & Planetary Science vol. 34 (1), pp. 25-41

Urquhart, M. L. & Mellon, M. T., 2007. "A New Model for Determining Lunar Rock Abundance and Landing Hazards". 38th Lunar and Planetary Science Conference, pp. 2171

Vasavada, A. R. et al, 1999. "Near-Surface Temperatures on Mercury and the Moon and the Stability of Polar Ice Deposits". Icarus Vol. 141, pp. 179-193

Ward, W. R., 1975. "Past Orientation of the Lunar Spin Axis". Science Vol. 189, pp. 377-379

Watson, K. et al, 1961. "The Behaviour of Volatiles on the Lunar Surface". J. Geophys. Res. Vol. 66, pp.3033-3045

Willman, B. M. et al, 1995. "Properties of Lunar Soil Simulant JSC-1". Journal of Aerospace Engineering Vol. 8 (2), pp. 77-87

11 Appendix

11.1 Bulk Parameters of the Moon and Earth

	Moon	Earth	Ratio (Moon/Earth)
Mass (10^{24} kg)	0.07349	5.9736	0.0123
Volume (10^{10} km^3)	2.1958	108.321	0.0203
Equatorial radius (km)	1738.1	6378.1	0.2725
Polar radius (km)	1736	6356.8	0.2731
Volumetric mean radius (km)	1737.1	6371	0.2727
Ellipticity (Flattening)	0.0012	0.00335	0.36
Mean density (kg/m^3)	3350	5515	0.607
Surface gravity (m/s^2)	1.62	9.8	0.165
Surface acceleration (m/s^2)	1.62	9.78	0.166
Escape velocity (km/s)	2.38	11.2	0.213
GM (x 10^6 km^3/s^2)	0.0049	0.3986	0.0123
Bond albedo	0.11	0.306	0.36
Visual geometric albedo	0.12	0.367	0.33
Visual magnitude V(1,0)	0.21	-3.86	-
Solar irradiance (W/m^2)	1367.6	1367.6	1
Black-body temperature (K)	274.5	254.3	1.079
Topographic range (km)	16	20	0.8
Moment of inertia (I/MR^2)	0.394	0.3308	1.191

Table 4: Bulk Parameters of the Moon and Earth (Data taken from the NASA National Space Science Data Centre, available from: http://nssdc.gsfc.nasa.gov/planetary/factsheet/moonfact.html).

11.2 Orbital Parameters of the Moon

	Moon
Semimajor axis (10^6 km)	0.3844
Mean Perigee (10^6 km)	0.3633
Mean Apogee (10^6 km)	0.4055
Revolution period (days)	27.3217
Synodic period (days)	29.53
Mean orbital velocity (km/s)	1.023
Max. orbital velocity (km/s)	1.076
Min. orbital velocity (km/s)	0.964
Inclination to ecliptic (deg)	5.145
Inclination to equator (deg)	18.28 - 28.58
Orbit eccentricity	0.0549
Sidereal rotation period (hrs)	655.728
Obliquity to orbit (deg)	6.68
Recession rate from Earth (cm/yr)	3.8

Table 5: Orbital parameters, for orbit about the Earth (Data taken from NASA NSSDC).

11.3 Properties of the Lunar Atmosphere

Diurnal temperature range	>100 K to <400 K
Total mass of atmosphere	~25,000 kg
Surface pressure (night)	3×10^{-15} bar
Abundance at surface	2×10^{5} particles/cm^3

Table 6: Lunar Atmospheric Properties (Data taken from NASA NSSDC).

11.4 Estimated Lunar Composition

Element/molecule:	**Particles/cm^3**
Helium 4 (^{4}He)	40000
Neon 20 (^{20}Ne)	40000
Hydrogen (H_2)	35000
Argon 40 (^{40}Ar)	30000
Neon 22 (^{22}Ne)	5000
Argon 36 (^{36}Ar)	2000
Methane	1000
Ammonia	1000
Carbon Dioxide	1000
Oxygen (O^+)	Trace
Aluminum (Al^+)	Trace
Silicon (Si^+)	Trace

Table 7: Estimated Composition of most abundant atmospheric species. Also possible traces of Phosphorus (P+), Sodium (Na+), Magnesium (Mg+) (Data taken from NASA NSSDC).

11.5 DLRE Specification Requirements

DLRE-L2-4	DLRE must be capable of measuring surface brightness temperature with an accuracy of 5K from 40 to 55K, 2.5K from 55 to 75K, and 1K from 75 to 300 K.
DLRE-L2-5	DLRE must be capable of measuring nighttime emitted thermal radiation of surfaces with temperature as low as 70K in at least two non-overlapping spectral channels that have brightness temperature accuracy better than 2.5K.
DLRE-FRD-66	The radiometric performance requirements summarized below shall apply to all 21 detectors in each DLRE spectral channel.
DLRE-FRD-68	In the DLRE thermal and mineralogy channels (A3, A4, A5, A6, B1, B2, and B3) the response to a 300 K blackbody source shall be calibrated to an absolute radiometric accuracy of better than ± 0.5% or to the noise level, whichever is larger.
DLRE-FRD-70	For the thermal channels, response to radiance from targets between 40 K and 400 K shall be characterized to better than ± 0.1% of the reference radiance or to the noise level, whichever is larger. For the mineralogy channels, response to radiance from targets between 200 K and 400 K shall be characterized to better than ± 0.1% of the reference radiance or to the noise level, whichever is larger.
DLRE-FRD-83a	Nominal signal-to-noise ratios and other performance parameters are listed in Table 3-2. Signal to noise ratios for channels B1-B3 shall be no less than 80% of these values. Signal to noise ratios for channels A3-A5 shall be no less than 80% of these values. Signal to noise ratios for channel A6 shall be no less than 50% of these values. It shall be acceptable for the requirements for optical transmission or detector D* not to be met for a given channel, provided the signal-to-noise requirement is met.
DLRE-FRD-236	When viewed by the DLRE telescopes, the effective emissivity of the blackbody calibration target shall exceed 0.992 for the mineralogy spectral bands, 0.986 for the 12.5-25 micron band, 0.978 for the 25-50 micron band, 0.970 for the 50-100 micron band, and

	0.965 for the 100-200 micron band. The emissivity values are averages over the spectral ranges weighted by a 300 K Planck distribution.

Table 8: The specifications of the DLRE instrument, required to be verified during pre-flight calibration [Foote, personal communication 2008].

11.6 The Brüker IFS 66v Fourier Transform Spectrometer

The Bruker IFS 66v and associated additions provides the capability to perform many types of filter and mineral measurements. Figure 40 shows the optical layout of the IFS 66v, with the major parts labelled. The system is capable of measuring a large portion of the spectrum, from the visible to the far infrared (FIR), using combinations of various radiation sources, windows, and beamsplitters:

- For visible and near infrared (NIR) measurements, a quartz-halogen bulb was used as the source, in conjunction with quartz windows and a Si diode detector.
- In the mid infrared (MIR), a Tungsten Globar^{TM} source was used with KBr windows and a Deuterated Triglycine Sulfate (DTGS).
- A FIR DTGS detector with Mylar beamsplitter was used with the Tungsten Globar^{TM} source for far infrared measurements.

Performing just these three measurements alone tends to measure only three distinct regions of the spectrum, so to record across the entire spectrum possible, combinations of sources and detectors can be used. For example, using the MIR detector and NIR beamsplitter, or vice versa, can measure the region of the spectrum between the usual NIR and MIR. A Specac^{TM} Diffuse Reflectance Accessory or Perkin Elmer^{TM} specular reflectance kit can be placed in the spectrometer sample compartment for making reflectance measurements, or a custom-built filter holder used to measure filter transmission. For emission measurements, an external emission port is available, with motorised mirrors to switch between the quartz-halogen, Globar^{TM} and external emission port.

The spectrometer can be evacuated to an ultimate pressure of approximately 20 mbar, so to achieve very low pressures of approximately 10^{-3} mbar, a vacuum chamber is required to be placed in the spectrometer sample compartment, with suitable windows attached to the ports.

To achieve the best signal possible, the signal hitting the detector needs to be maximised. This is achieved by moving the aperture wheel to the largest possible aperture size where:

- The inteferogram does not saturate the detector, or
- The beam does not extend beyond the object being measured.

To increase the signal further on the DTGS and FIR DTGS detectors, the velocity of the scan mirror can be decreased, though this increases the time taken to make a measurement. Then, if on the largest aperture and slowest velocity possible, the amplitude of the interferogram is still small, the gain of the detector can be increased. An appropriate number of scans is performed depending on the quality of the interferogram observed, with the error in the resulting measurement decreased by the square root of the number of scans.

Optimising the alignment of the mirrors is achieved by running the “auto align” algorithm in the software. This is performed several times per day, and after every beamsplitter change.

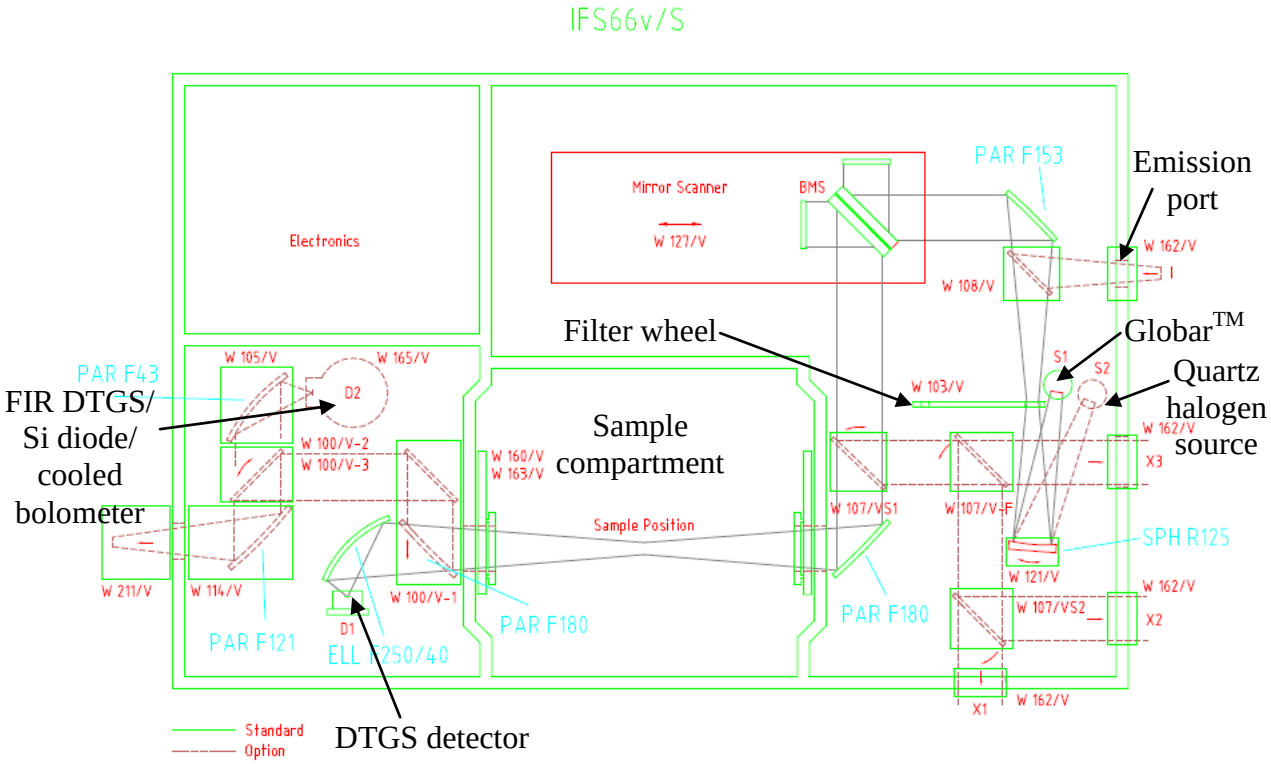

Figure 40: The optical layout inside the Brüker IFS 66v Fourier Transform Spectrometer, with the main parts labelled. Almost all of the optional parts (dotted red line) are available.